Research Square

Preprints are preliminary reports that have not undergone peer review.
They should not be considered conclusive, used to inform clinical practice,
or referenced by the media as validated information.

Magnetic Particle Imaging in Human Subjects

Erica Mason

erica.mason.phd@gmail.com

Magnetic Insight, Inc. https://orcid.org/0000-0001-7002-3599

Olivia Sehl

Magnetic Insight, Inc. and Western University, Robarts Research Institute

Marcela Weyhmiller

Magnetic Insight, Inc.

Bryanna Davison

Magnetic Insight, Inc.

Eli Mattingly

Magnetic Insight, Inc.

Justin Konkle

Magnetic Insight, Inc. https://orcid.org/0000-0003-1198-049X

Toby Sanders

Magnetic Insight, Inc.

A. Mohtasebzadeh

Magnetic Insight, Inc.

Elliott Barcikowski

Magnetic Insight, Inc.

Kyle Fields

Magnetic Insight, Inc.

Chris Raanes

Magnetic Insight, Inc.

Nitara Fernando

Western University, Robarts Research Institute

Carlos Rinaldi-Ramos

University of Florida, Department of Chemical Engineering and J. Crayton Pruitt Family Department of Biomedical Engineering https://orcid.org/0000-0001-8886-5612

Osama Mawlawi

University of Texas MD Anderson Cancer Center, Department of Imaging Physics

Paula Foster

Western University, Robarts Research Institute

Andreas Loening

Stanford University, Department of Radiology https://orcid.org/0000-0003-3316-7467
Eric Padua
Magnetic Insight, Inc.
Stephan Lai
The University of Texas MD Anderson Cancer Center
Max Wintermark
University of Texas MD Anderson Cancer Center, Department of Neuroradiology
Patrick Goodwill
Magnetic Insight, Inc. https://orcid.org/0000-0003-4240-1956

Article

Keywords:

Posted Date: March 17th, 2026

DOI: https://doi.org/10.21203/rs.3.rs-8825005/v1

License: This work is licensed under a Creative Commons Attribution 4.0 International License.
Read Full License

Additional Declarations: Yes there is potential Competing Interest. At the time of the study, all authors employed by Magnetic Insight, Inc. were stockholders in the company. Magnetic Insight, Inc. is no longer in business at the time of manuscript submission.

Magnetic Particle Imaging in Human Subjects

Erica E. Mason[1]*,
Olivia C. Sehl[1,2]*,
Marcela G. Weyhmiller[1],
Bryanna Davison[1],
Eli Mattingly[1],
Justin J. Konkle[1],
Toby Sanders[1],
A. Rahman Mohtasebzadeh[1],
Elliott Barcikowski[1],
Kyle Fields[1],
Chris A. Raanes[1],
Nitara Fernando[2],
Carlos M. Rinaldi-Ramos[3],
Osama Mawlawi[4],
Paula J. Foster[2],
Andreas M. Loening[5],
Eric M. Padua[1],
Stephen Y. Lai[6],
Max Wintermark[7],
Patrick W. Goodwill[1]

* Co-first author

1 Magnetic Insight Inc., Alameda, CA

2 Department of Medical Biophysics, Western University, Robarts Research Institute, London, ON

3 Department of Chemical Engineering and J. Crayton Pruitt Family Department of Biomedical Engineering, University of Florida, Gainesville, FL

4 Department of Imaging Physics, University of Texas MD Anderson Cancer Center, Houston, TX

5 Department of Radiology, Stanford University, Stanford, CA

6 Department of Head and Neck Surgery, University of Texas MD Anderson Cancer Center, Houston, TX

7 Department of Neuroradiology, University of Texas MD Anderson Cancer Center, Houston, TX

Abstract

Magnetic Particle Imaging (MPI) is a tracer-based medical imaging modality that detects magnetic nanoparticles with no background tissue signal. MPI acquires quantitative, high-sensitivity tomographic images of shelf-stable magnetic tracers that safely produce signals *in vivo* for weeks or even months. These features can fill capability gaps in medical imaging for applications benefiting from tracer specificity with an extended imaging window. Despite two decades of preclinical validation and multiple published human-scale imagers, MPI has not previously been demonstrated in human subjects. Here we report MPI imaging in two subjects following subcutaneous administration of magnetic tracer in the scalp and foot. Our results showed quantitative and longitudinal visualization of lymphatic drainage for up to six months, with

supporting validation in a mouse model. Imaging in human subjects required the development and verification of a novel clinical imager, including magnetostimulation threshold testing of all magnetic fields used in imaging sequences. To understand MPI in the context of existing medical imaging technologies, we benchmarked MPI imaging performance against SPECT using lymphatic system phantom models. These findings demonstrate that MPI can translate from animals to human subjects, and establish MPI as a new tool for longitudinal tracer imaging in medicine. The addition of MPI to the clinical imaging toolbox could enable new approaches and capabilities for diagnosis, real-time interventions, and treatment monitoring across a broad range of clinical applications.

Introduction

Magnetic Particle Imaging (MPI) is a tracer imaging modality that detects magnetic nanoparticles with no signal from biological tissue. MPI fills a capability gap of existing clinical imaging by sensitively, specifically, and quantitatively imaging a magnetic tracer for weeks to months[1,2]. This unique combination of capabilities contrasts with radiotracer-based imaging, where hour-long decay half-lives can constrain applications and workflows. For example, MPI has demonstrated preclinical visualization of sentinel lymph nodes for days to weeks[3], and may provide an alternative to the constrained imaging windows used in lymphoscintigraphy requiring careful coordination of tracer injection, imaging, and surgery[4–6]. MPI excels at long-term tracking of adoptive cell therapies including T cells[7,8], natural killer cells[9], dendritic cells[10], and stem cells[11,12]. The technology has also been demonstrated for immune and inflammation imaging[13,14], targeted imaging of checkpoint inhibitor receptor density[15], treatment planning for magnetic hyperthermia[16,17], functional brain imaging in rats[18] and non-human primates[19,20], interventional imaging in human leg cadaver specimens[21], and even directly detecting endogenous hemosiderin to identify unstable plaques[22].

First published by Gleich and Weizenecker[23] and in patent literature[24], MPI measures the nonlinear magnetization response of magnetic tracers such as superparamagnetic iron oxide nanoparticles (SPIOs). A selection field gradient magnetically saturates the tracer throughout the imaging volume except in a small field-free region where time-varying drive fields cause unsaturated magnetic tracer to traverse a nonlinear magnetization curve and induce a voltage signal in receiver coils[23,25]. Magnetic saturation outside the field-free region ensures that signals originate only from the field-free region, which is scanned across the sample to generate images (**Extended Data Figure 1a**). Signal intensity is linearly proportional to magnetic tracer concentration, providing both quantitative accuracy and tracer specificity with no background signal[26]. These magnetic tracers maintain a signal over weeks to months, enabling sustained longitudinal studies that eliminate the temporal constraints of radiotracer-based imaging[27].

MPI in human subjects has not been previously published, despite two decades of preclinical validation, human-scale imager development, and basic safety testing[28]. Here we report imaging of the head-and-neck and foot in two human subjects on a novel clinical MPI scanner following subcutaneous administration of magnetic tracer, and demonstrate quantitative, longitudinal lymphatic imaging showing tracer localization in lymph node regions. Human subject imaging was enabled by key technical innovations in the scanner design and verification of the system including subject-specific magnetostimulation threshold testing. The human imaging results are additionally supported by a phantom study to benchmark MPI performance against clinically-available modalities, and a mouse study to validate the translation of MPI from preclinical to clinical. In total, the results reported here validate MPI as safe and clinically translatable, with lymphatic imaging as the first demonstrated application.

Results

To translate MPI to human scale, we designed, built, characterized, and verified the basic safety of a human MPI imaging system, and longitudinally imaged human subjects following magnetic tracer injection (**Figure 1, Extended Data Figures 1-7**). Basic safety (defined in **Methods**) testing included SAR testing in phantoms (**Figure 1b**) and magnetostimulation threshold testing in 6 healthy subjects (4 heads–**Figure 1c**; 6 feet–not shown). We subcutaneously injected ferumoxytol, an FDA-approved[29,30] SPIO, into 2 healthy subjects (2 heads–**Figure 1d,e**; 2 feet–not shown). Tomographic MPI imaging was performed and co-registered with optical surface scans for both subjects (**Figure 1f,g; Supplemental Video SV1; Supplemental Data SD1,SD2**), at time points up to six months after injection (**Figure 1h**). The head-and-neck images showed magnetic tracer at injection sites and at lymph node regions within the field of view. Each subject had a unique lymphatic drainage pattern to periauricular and cervical lymph node regions, which agrees with known lymphatic anatomical pathways from the parietal scalp[4,31–33]. Both subjects showed signal in the cervical lymph node region that was confirmed by repeated imaging with the subject rotating their head and by moving the surface coils superior-inferior (**Extended Data Figure 7**). The system achieved sufficient dynamic range and shine-through performance to visualize injection sites and lymph node regions simultaneously. The imaging procedures, with each scan lasting up to 20 minutes, were well-tolerated with no adverse events related to the use of the clinical imager. Tracer administration resulted in expected mild skin discoloration[34] at all injection sites (**Figure 1d**, **Extended Data Table 2a**, **Supplementary Figure S1**) and resolved within weeks. One subject (S04, 1 mL injection volume) experienced mild pain during injection in the parietal scalp, which resolved immediately (**Extended Data Table 2a**).

To assess MPI's unique longitudinal and quantitative capabilities, we quantified the pharmacokinetics of the tracer in the head and foot within regions of interest for up to six months (**Figure 2, Extended Data Table 2**). Following subcutaneous injection in the parietal scalp, MPI signal was detected at the injection site, which cleared over time (**Figure 2b**), and in periauricular and cervical lymph node regions, which showed an increase in signal for 48 hours and then a gradual decay over several weeks (**Figure 2d**). After tracer injections in the foot posterior to the lateral malleolus, signal was detected at the injection site and decayed over time (**Figure 2c**), but no signal from the lymph nodes is reported as the draining popliteal and inguinal lymph node regions could not be positioned within the scanner's field of view. The MPI signal decay at both injection sites and head and neck lymph node regions fits well to bi-exponential kinetics characterized by fast and slow phases (best-fit parameter estimates reported in **Extended Data Table 2b**). At each anatomical location, the higher-dose injection site signal exhibited a faster initial clearance rate than the lower dose, potentially due to the larger injection volume. At each dose, the foot injection site signal exhibited a faster initial clearance rate than the scalp.

Our clinical imager has a 25 cm imaging bore to fit the head and neck or extremities, and a field of view (FOV) of 24 × 24 × 30 cm to enable imaging from crown to laryngeal prominence (**Extended Data Figure 2,3,5**). The design utilized a multi-receive-coil architecture combining volume and surface coil arrays (**Extended Data Figure 5,6**). The application-specific surface coil arrays enable improved sensitivity and shine-through performance, and in this study are positioned close to the head and neck near the anatomical location of expected lymphatic drainage pathways. Prior to imaging, the imager was verified for basic safety and adherence to relevant FDA risk guidance for MRI (see **Methods**). We simulated and experimentally verified specific absorption rate (SAR), and tested magnetostimulation thresholds for peripheral nerve stimulation (PNS) and magnetophosphene perception (**Figure 3**). SAR was simulated for a human body model and a cylindrical phantom, and the phantom results were experimentally verified, which confirmed SAR to be below the threshold used in MRI for significant risk operating conditions (see **Methods**, **Figure**

3a,b). Thresholds for magnetostimulation were simulated up to 7 mT peak drive field (**Figure 3c**) and then experimentally tested up to the system's designed maximum drive field strength of 3.5 mT peak (**Figure 3d,e**) in 6 healthy subjects (4 heads, 6 feet) and again after magnetic tracer injection in 2 subjects (2 heads, 2 feet). In the head, one subject (n=1/4) experienced threshold magnetostimulation (PNS) at a drive field amplitude of 3.2 mT peak (50% probability), which occurred near an MRI compatible gold-alloy dental crown. In the foot, no subjects (n=0/6) experienced magnetostimulation. There was no detectable change in magnetostimulation threshold after magnetic tracer injection.

To benchmark MPI performance against standard clinical lymphatic imaging methods, we imaged anthropomorphic phantoms with MPI, planar scintigraphy, and SPECT (**Figure 4**). Two magnetic tracers were evaluated: ferumoxytol and ferucarbotran. With ferucarbotran, we observed image resolution comparable to [^{99m}Tc]tilmanocept SPECT, with MPI showing similar axial resolution (z) but lower transverse resolution (x,y). With ferumoxytol, MPI showed markedly worse resolution, as confirmed in phantoms (**Extended Data Figure 4**).

To further explore lymphatic imaging with MPI and compare tracer-dependent pharmacokinetics in vivo, we performed studies in healthy mice using ferumoxytol and ferucarbotran (**Figure 5**). MPI showed a rapid clearance of ferumoxytol from the injection site and uptake into multiple lymph node echelons before accumulating in the liver (**Figure 5c,d**). MPI signal in lymph nodes was detected as early as 1 hour after injection and persisted for at least 8 weeks (**Figure 5e**), and iron deposits were confirmed by *ex vivo* Prussian blue staining (**Figure 5f**). Ferumoxytol sold by AMAG Pharmaceuticals (n=7) and Sandoz (n=3) showed similar magnetic properties and lymph node deposition (**Figure 5a,f**). Ferucarbotran (n=6) exhibited slower clearance from the injection site and was detected in only the first draining sentinel lymph node, consistent with the reported pharmacokinetics of Magtrace[34–36].

The MPI hardware developed here has applications beyond clinical lymphatic imaging, outside the scope of our human study. In anticipation of future uses, we explored imaging phantom models of brain cancer, real-time embolization, and cerebral angiography (**Extended Data Figure 8, Supplemental Video SV2**).

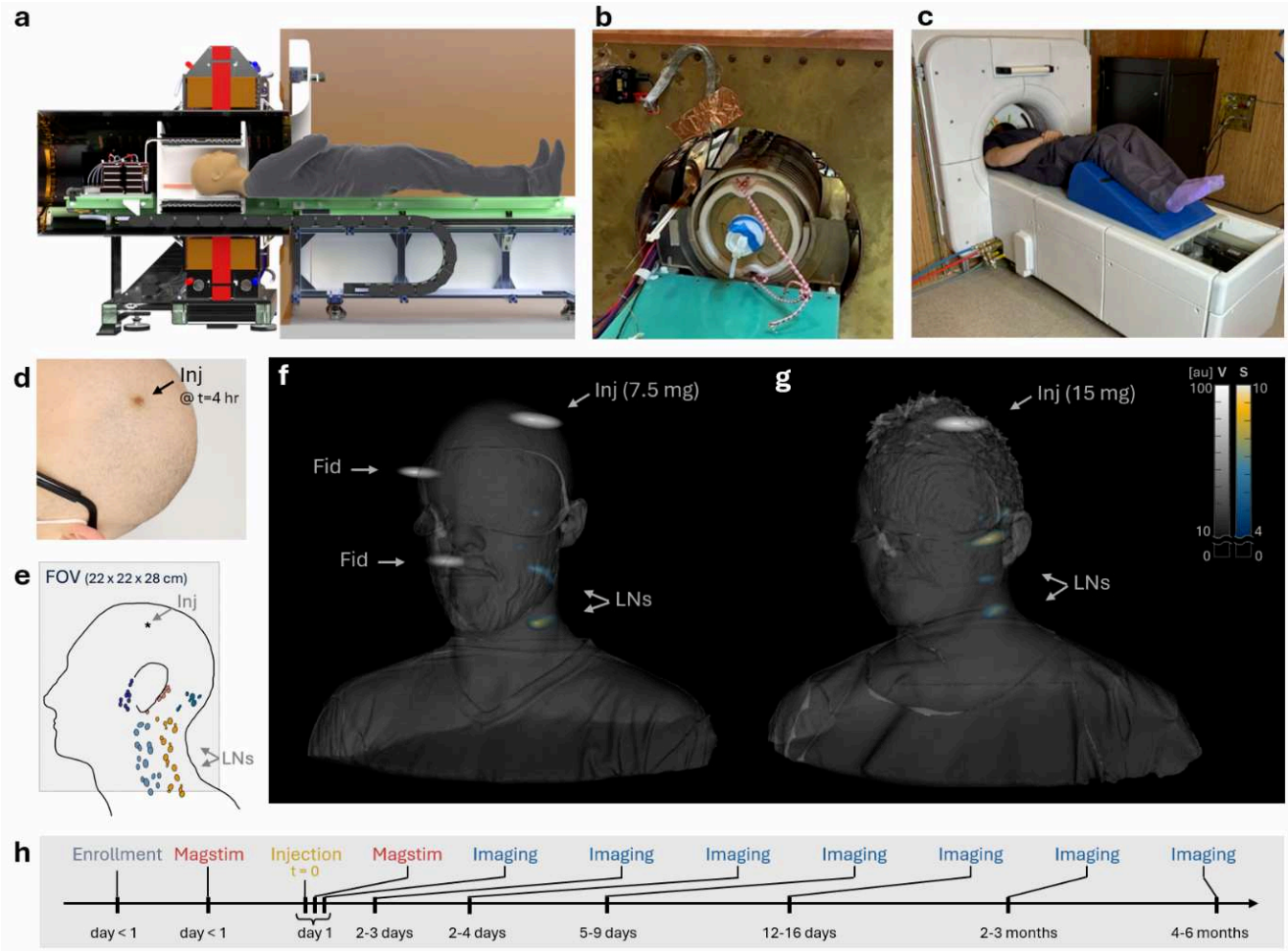


Figure 1: First-in-human magnetic particle imaging demonstration. **(a)** A head-and-neck MPI system was constructed and **(b,c)** verified for basic safety and against FDA criteria for significant risk investigations in MRI. **(b)** Specific absorption rate (SAR) testing was performed on phantoms. **(c)** Magnetostimulation threshold testing was conducted on the head (n=4) and foot (n=6, not shown) for all magnetic fields used in MPI sequences. **(d)** In a subset of subjects, tracer was injected subcutaneously in the scalp (n=2) and in the foot (n=2, not shown). **(e)** For the scalp injection, MPI images are acquired with FOVs that extend from beyond the crown to the laryngeal prominence, allowing imaging of the expected drainage paths in the periauricular and cervical regions[4,31–33] (illustration adapted from Gregoire *et al.* 2013)[31]. **(f,g)** Tomographic MPI images were generated by compositing data from multiple receiver coils, with volume coil images (V) shown in grayscale and application-specific surface coil images (S) shown in color (see also **Supplemental Video SV1, Supplemental Data SD1,SD2**). MPI volume renderings were co-registered with de-identified surface scans acquired using a hand-held 3D camera. **(f)** Image of subject with 7.5 mg ferumoxytol injection at t = 12.4 days, with two fiducials (Fid) containing 0.5 mg ferumoxytol. **(g)** Image of subject with 15 mg ferumoxytol injection at t = 28.5 hours, no fiducials used. **(h)** Representative timeline illustrating injection (t = 0), magnetostimulation before and after injection, and approximate imaging timepoints up to 6 months post-injection.

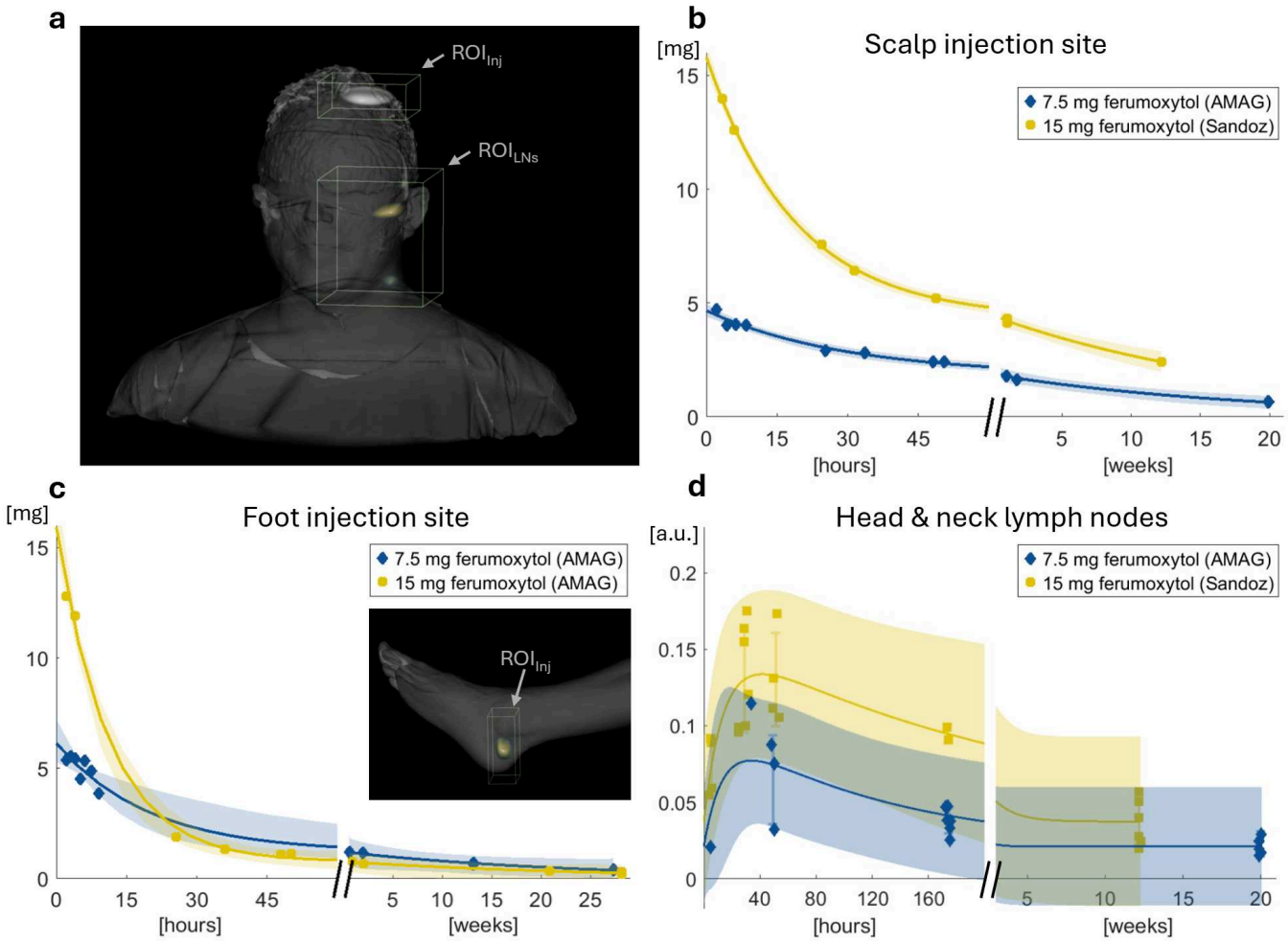
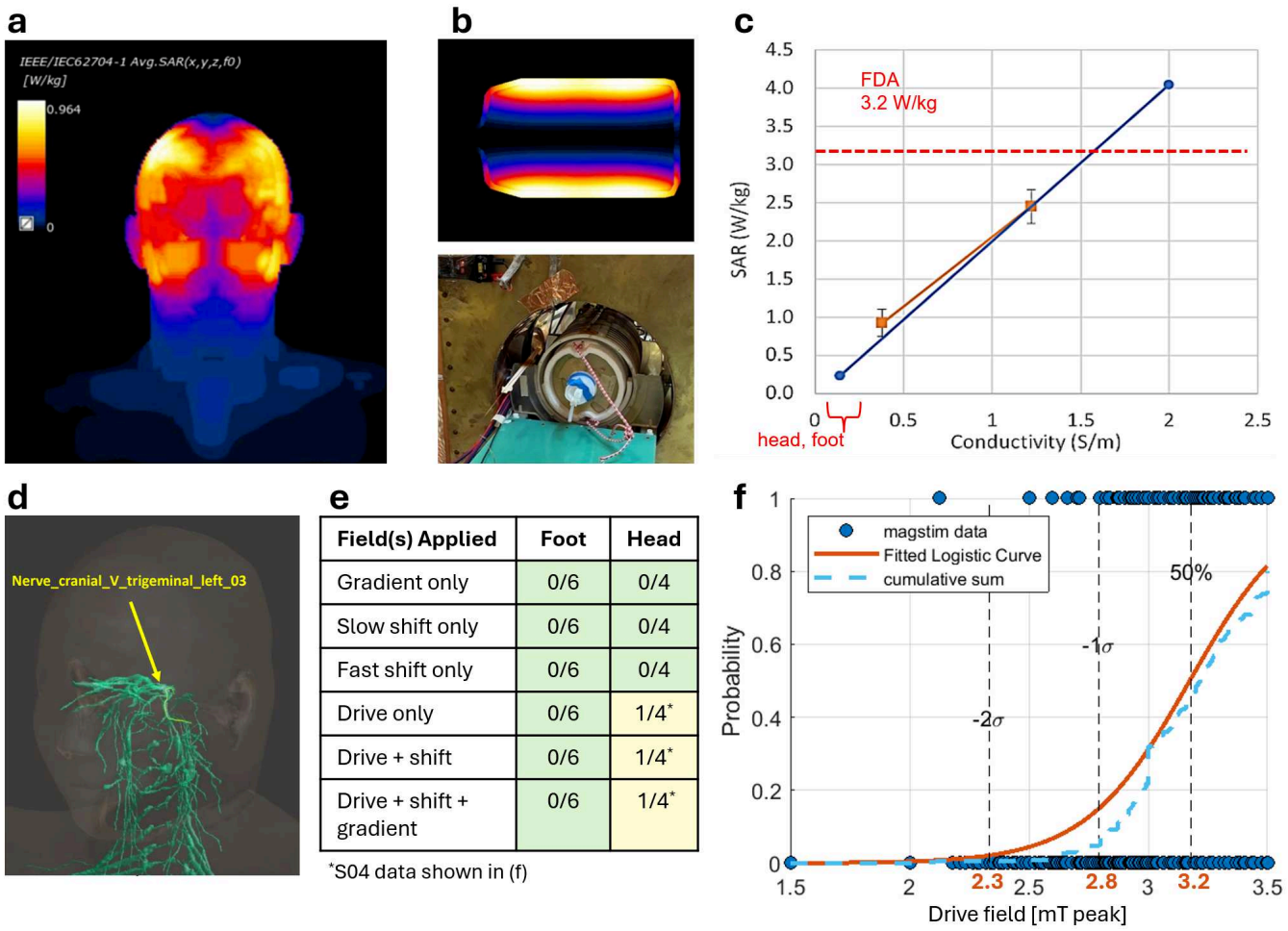


Figure 2: *In vivo* quantitative pharmacokinetics of iron oxide tracer in two healthy subjects. Data are displayed for 7.5 mg dose (blue diamonds) and 15 mg dose (yellow squares) and fit to a bi-exponential (solid lines) with 95% prediction intervals (shaded region). Time constants are reported in **Extended Data Table 2**. **(a)** Representative MPI image showing 3D regions of interest (ROIs) for quantification of injection site (Inj) and draining lymph node regions (LNs). **(b)** MPI signal at the scalp injection site over time. Data was calibrated with phantoms containing known iron concentrations. **(c)** Calibrated MPI signal at the foot injection site, with inset showing 3D ROI on a representative MPI scan of the foot. **(d)** MPI signal of accumulation and persistence in draining lymph node regions from the head injection. Because of varied scanning sequences and changing surface coil positioning during these exploratory first-in-human scans, lymphatic signal exhibits image-to-image variation and is presented in arbitrary units (a.u.) without calibration. Draining lymph node regions from the foot were unable to be positioned within the scanner's field of view.



Field(s) Applied	Foot	Head
Gradient only	0/6	0/4
Slow shift only	0/6	0/4
Fast shift only	0/6	0/4
Drive only	0/6	1/4*
Drive + shift	0/6	1/4*
Drive + shift + gradient	0/6	1/4*

*S04 data shown in (f)

Figure 3: Testing clinical MPI system for basic safety (defined in Methods) and FDA risk guidance for MRI. (a) We simulated SAR in the "Duke" virtual body model with a 7 mT peak drive field, which showed an average regional SAR in the head of 0.232 W/kg and a peak SAR of <1 W/kg, both of which are well below the FDA significant risk guidelines for MRI. **(b)** We also measured and simulated SAR in a cylindrical test phantom and **(c)** found good correspondence between the simulation and measurement. **(d)** Magnetostimulation simulation in the "McIntyre-Richardson-Grill" neuronal model predicts peripheral nerve stimulation (PNS) at the cranial V trigeminal nerve at a drive field amplitude of 2.8 mT peak. **(e)** The magnetostimulation test protocol was performed on healthy subjects (n=6 feet, n=4 heads). To determine subject-specific magnetostimulation thresholds and set scanning parameters for imaging, our protocol individually and combinatorically tested gradient, shift, and drive fields. The table indicates the number of healthy subjects that reported sensations of magnetostimulation in the foot or head for each set of fields. Only one subject (S04) experienced magnetostimulation during tests involving the drive field. **(f)** S04's magnetostimulation results are plotted and fit to a logistic regression to determine the 50% probability, 50%-1σ and 50%-2σ amplitudes. Since no gross differences in stimulation thresholds were experienced from the drive field in combination with additional fields or pre- versus post-injection, all of S04's drive field magnetostimulation results are pooled. The results are used to determine the maximum drive field amplitude for use in this subject's image sequences.

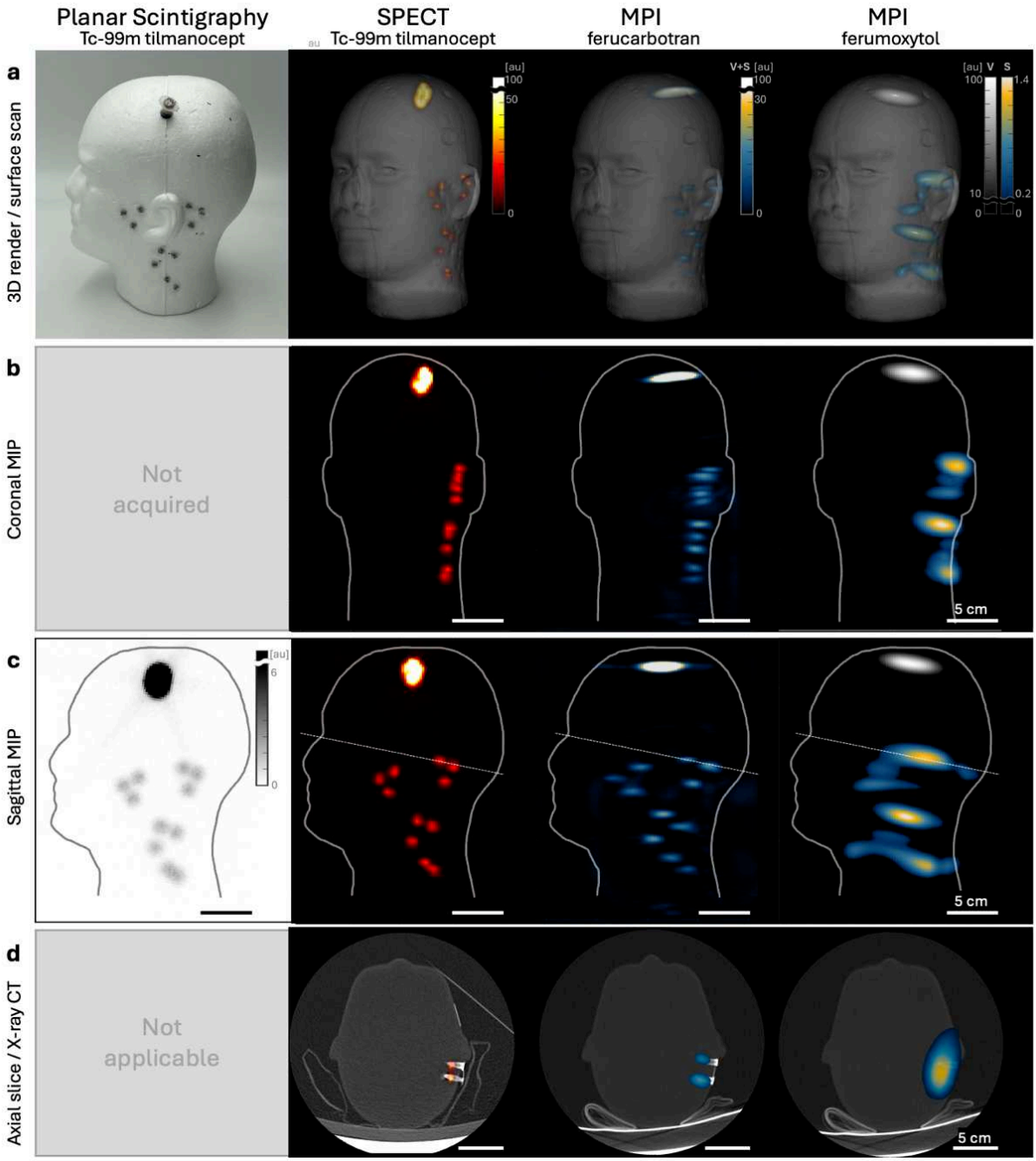


Figure 4: Clinical performance benchmarking of MPI against standard-of-care nuclear imaging. A lymph node head-and-neck phantom containing a 1.5 mL Eppendorf tube in the parietal scalp and 11× 0.2 mL Eppendorf tubes in the periauricular and cervical lymph node regions. The phantom was filled with a 100:1 tracer quantity difference between mock injection and lymph nodes, with [^{99m}Tc]tilmanocept for planar scintigraphy and SPECT or with ferucarbotran or ferumoxytol for MPI. Scale bars represent 5 cm. **(a)** Photograph of phantom, and 3D volume rendering of SPECT and MPI images co-registered with an optical surface scan. **(b)** Coronal maximum intensity projection (MIP) of SPECT and MPI (not acquired for planar scintigraphy). **(c)** Sagittal MIPs of SPECT and MPI, and sagittal projection of planar scintigraphy. **(d)** Oblique axial slice of SPECT/CT and MPI/CT at the dotted-line drawn in (c) (not applicable for planar scintigraphy).

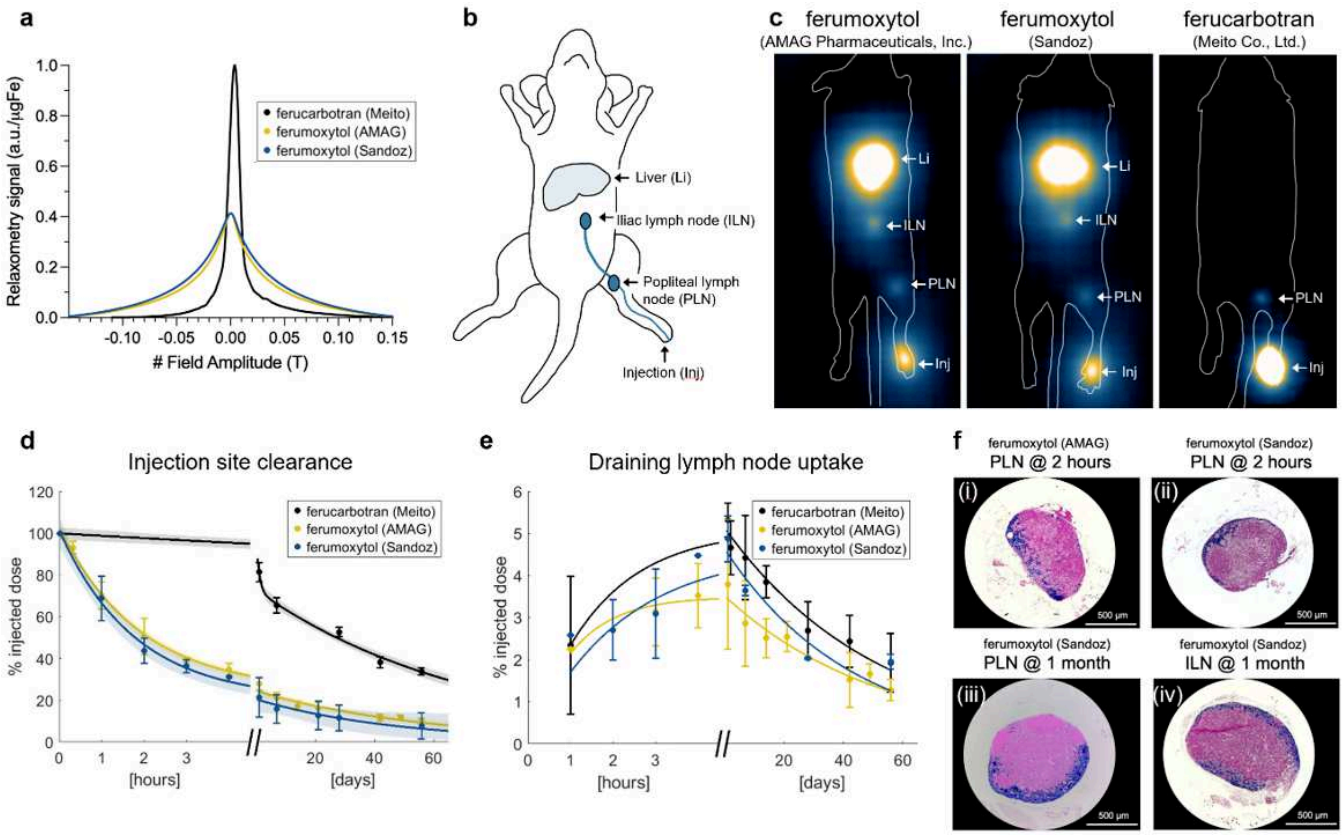


Figure 5: Tracer properties drive magnetic and pharmacokinetic performance, demonstrated in an *in vivo* mouse model with histological confirmation. (a) MPI relaxometry measures the signal strength (maximum) per µg Fe, and resolution (full width at half maximum) for each tracer. Ferumoxytol shows ~40% lower signal strength and 5-6× worse resolution compared to ferucabotran, with minimal differences between ferumoxytol manufacturers. **(b)** Mouse lymphatic anatomy showing footpad injection site (Inj) and expected draining nodes[37]. **(c)** Full-body mouse MPI shows biodistribution of ferumoxytol (AMAG Pharmaceuticals) (n=7), ferumoxytol (Sandoz) (n=3), and ferucarbotran (Meito Co., Ltd.) (n=3), 24 hours after tracer injection to the mouse footpad. Magnetic tracers are detected in the draining popliteal lymph node (PLN), secondary iliac lymph nodes (ILN), and liver (Li). **(d,e)** Longitudinal quantification of MPI signal, where time-series data are fit to a bi-exponential (solid lines) with 95% prediction intervals (shaded region), shows **(d)** rapid clearance of ferumoxytol (AMAG and Sandoz) from the injection site and **(e)** accumulation in lymph nodes within 4 hours and for 8 weeks. Comparatively, ferucarbotran shows slower clearance kinetics and accumulation in lymph nodes was detected by MPI after 24 hours. **(f)** Perl's Prussian blue staining confirms iron staining following ferumoxytol injection, in excised draining PLN at (i) 2 hours after AMAG product, (ii) 2 hours after Sandoz product, (iii) 1 month after AMAG product, and (iv) in the ILN at 1 month after Sandoz product. Scale bars = 500 µm.

Discussion

First-in-human images with MPI represent a milestone in medical imaging, demonstrating translation of an emerging tracer imaging modality to clinical research. Until now, no images of human subjects have been reported[28]. We showed longitudinal and quantitative visualization of magnetic tracer pharmacokinetics in humans, with sufficient sensitivity and resolution for clinical applications that can benefit from these capabilities such as presurgical imaging for sentinel lymph node biopsies. These milestones were reached safely in healthy subjects. MPI's unique technical characteristics open new applications benefiting from hotspot image contrast, weeks-long signal half-life, shelf-stable tracers, and no ionizing radiation.

MPI has evolved over two decades; preclinical MPI is commercially available[38], and several human-scale prototype scanners have been developed[39–44]. These scanners have imaged non-human primates[19,20] and human cadaver leg specimens[21], but until now, no images of human subjects have been reported. To achieve human MPI images, we constructed novel hardware, and designed and verified it following a risk-based approach for use in an Institutional Review Board approved study. The hardware is sized for head-and-neck (field of view of 24 × 24 × 30 cm), and achieves the sensitivity, dynamic range, and shine-through performance sufficient for lymph node imaging applications.

Our study established MPI's clinical feasibility by demonstrating lymphatic imaging, where MPI can fill gaps in current clinical workflows and capabilities. The most used lymphatic imaging technique, the sentinel lymph node biopsy (SLNB) guided by ^{99m}Tc radiotracer-based imaging, is widely used for staging early-stage breast cancer, melanoma, and head-and-neck malignancies[4,6,32,45]. The short half-life of ^{99m}Tc (6 hours) necessitates same or next day coordination of tracer injection, presurgical imaging, and surgery[4]. Emerging magnetic SLNB methods using iron oxide nanoparticles and handheld magnetic probes eliminate this timing constraint, allowing at least 7 days between injection and surgery[46], but lack presurgical imaging capability and are limited to use in patients with breast cancer[35].

Here we demonstrate MPI lymphatic visualization, with the goal of supporting presurgical imaging for magnetic SLNB workflows in melanoma and head and neck cancer, where imaging remains essential for surgical planning as drainage patterns are complex and variable[4,32]. The human MPI scanner achieved sufficient sensitivity, dynamic range, and shine-through performance to visualize magnetic tracer pharmacokinetics in the lymphatic system with no background signal arising from tissues (**Figure 1**). We acquired MPI images of two subjects with subcutaneously injected magnetic tracer in parietal scalp, and detected MPI signal in periauricular and cervical lymph node regions (**Extended Data Figure 7**), consistent with prior MR lymphangiography studies performed by the authors utilizing ferumoxytol (unpublished data). Quantification of magnetic tracer was performed in humans for up to 28 weeks (**Figure 2**). We then tested image quality in phantoms across modalities and tracers, and found that MPI with ferucarbotran, a tracer shown to have suitable axillary sentinel lymph accumulation for intraoperative surgical guidance using a handheld detector[47], has comparable image quality to planar gamma camera and SPECT with [^{99m}Tc]tilmanocept at clinically relevant tracer quantities (**Figure 4**). These findings are supported by preclinical mouse studies (**Figure 5**), which establish biological validation, cohort-level robustness, and scalability of lymphatic MPI from mice to humans.

Although clinical MPI systems and tracers are in their first generation, in **Figure 4** we benchmark MPI against state-of-the-art SPECT and planar scintigraphy. The phantoms were designed to represent and approximate lymph node anatomy draining from a melanoma site in the parietal scalp[31–33]. The magnetic and radiotracer phantom were both filled with a 100:1 tracer quantity ratio between a mock injection site and draining lymph nodes, modeling approved tracer doses[35,48] and reported deposition in lymph nodes[49–51] (**Figure 4**). The imaging results highlight the importance of tracer selection on imaging performance. With

ferucarbotran, MPI achieves comparable image quality to SPECT with [^{99m}Tc]tilmanocept, with similar per node detectability. On the other hand, ferumoxytol, the tracer used in our human subjects, showed approximately 5-fold worse spatial resolution than ferucarbotran on identical hardware (**Extended Data Figure 4,5a**). This difference arises because MPI spatial resolution depends on the magnetic nanoparticle's magnetization curve steepness in addition to hardware specifications[1]. Compared to ferumoxytol, ferucarbotran has larger magnetic core size which produces steeper magnetization transitions and correspondingly better image quality[2,13]. Our phantom data establish that future MPI studies using ferucarbotran or purpose-designed tracers should achieve substantially improved spatial resolution without changing hardware specifications[52,53]. As MPI hardware and tracers mature, we expect imaging performance to improve in field of view, sensitivity, resolution, and dynamic range, similar to how MRI, CT, and nuclear medicine evolved rapidly in the 1970s and 1980s.

Our preclinical studies (**Figure 5**) were integral to the design of the human imaging protocol and provided independent biological validation of human lymphatic imaging. Mouse data informed study design by confirming ferumoxytol visibility with MPI, establishing expected pharmacokinetic behavior with whole-body context, and guiding selection of imaging time points. In mice, ferumoxytol reproducibly cleared rapidly from the injection site and accumulated in multiple lymph node echelons within hours, with quantitative signal stability persisting for at least 8 weeks, consistent with trends observed in human subjects. Notably, the circulation dependent decay rate (τ_1) has a ~10-fold difference between mouse and human, which is consistent with the expected allometric scaling of circulation time (M^0.25)[54] (**Extended Data Table 2**). The mouse model enabled direct validation of imaging findings through excision of lymph nodes and histological confirmation of iron deposition, providing biological ground truth that is not feasible in human studies. Mouse imaging also supported the interchangeability of brand-name and generic ferumoxytol used in the human study. Finally, it enabled a direct comparison of the pharmacokinetic behavior of ferumoxytol and ferucarbotran, which have different coatings and hydrodynamic diameters (17-31 nm[29] and ~57 nm[47], respectively), highlighting tracer-dependent pharmacokinetic variability and informing future tracer selection. While we did not inject ferucarbotran into human subjects, these preclinical studies reaffirm that it is suitable as a sentinel lymph node magnetic tracer[3,49], accumulating primarily in the first nodal echelon. Together, the strong concordance between mouse and human results strengthens confidence in translating MPI from small-animal models to broader clinical applications.

Human translation required a novel main magnet. In order to achieve an axial FOV from the crown to the laryngeal prominence, the system was designed with a 55 cm free bore to fit the shoulders and torso, allowing shifting of the subject through the isocenter (**Extended Data Figure 2,3**). This main magnet design can scale to whole-body imaging systems, with larger bores and extended axial coverage while maintaining a field gradient greater than 0.5 T/m.

Many clinical applications, including lymphatic imaging, benefit from strong shine-through performance, which is the ability to resolve small signal sources nearby a large source. We improved shine-through performance using a unique combination of volume and surface receive coils, where multi-channel volume coils enable large fields of view with uniform receive profiles and application-specific surface coils provide localized high sensitivity (**Extended Data Figure 5,6**). We note that shine-through performance relies on having sufficient imager dynamic range, which is the ratio of the largest to smallest signals that can be imaged in isolation, and can span 4-6 orders of magnitude before detector saturation occurs. In our study, the application-specific surface coil arrays were placed in close proximity to the expected lymphatic drainage basin, both improving dynamic range and reducing shine-through artifact when visualizing milligram-level injection sites next to microgram-level lymph node accumulation. These coils are used throughout our human study, and when used with ferucarbotran in our SLN phantom can visualize an 8000:1 tracer ratio between injection site and lymph nodes, which exceeds expected physiologic dynamic range by at least an

order of magnitude (**Extended Data Figure 6d**).

Our study had several limitations. Our testing with ferumoxytol did not demonstrate human imaging at MPI's full imaging performance capabilities, and future clinical tests using optimized tracers are expected to achieve substantially better image quality than demonstrated here (**Figure 4**, MPI ferucarbotran versus MPI ferumoxytol). While Magtrace, an FDA-approved medical device for SLNB procedures[35] has performance similar to ferucarbotran (data not shown), it was not available for our study; ferumoxytol was readily available and was used off-label from its FDA-approved indications as an iron replacement therapy and for cancer neuroimaging[29,30]. As a healthy subject study, *in vivo* imaging comparisons with existing clinical modalities was not justified, particularly those necessitating radioactive tracer administration. We instead relied on phantoms to compare relative performance of MPI with scintigraphy and SPECT (**Figure 4**). In future MPI studies in patient populations, dual tracer techniques may be warranted and would enable magnetic versus nuclear imaging comparisons. Nodal biopsy in healthy subjects was also not justified, and so to confirm localization of MPI signal in lymph node regions, we relied on imaging experiments that show tracer signal follows anatomy when repositioning the subject or receiver coils (**Extended Data Figure 7**). Our small sample size (n=4 experiments with tracer injection, n=10 experiments for magnetostimulation threshold testing) provided limited statistical power for assessing inter-subject variability, though consistency between subjects and agreement with mouse data suggest reproducibility. The magnetostimulation threshold testing served its primary purpose to set subject-specific parameters for imaging sequences, but as it was only performed up to 3.5 mT peak and only achieved thresholds in one subject (at a location of prior dental work), it does not provide generalizable results. Last, the imager's field of view restricted imaging to head and neck anatomy, precluding assessment of lymph node regions inferior to the laryngeal prominence. We also were unable to image the extent of the foot lymphatic basin including popliteal or inguinal lymph nodes[55] that we were unable to position within the imaging region.

MPI addresses an unmet need in tracer imaging beyond lymphatic imaging with radiation-free, quantitative, sensitive, and sustained measurements. With existing tracers approved for human use and the scanner technology developed here, MPI may already be able to supplement or replace MRI, X-ray, and radiotracer-based studies. For example, ferumoxytol recently received FDA approval for brain tumor imaging with MRI[30] (Ferabright^{TM}, Azurity Pharmaceuticals), and MPI could provide complementary directly quantitative measurements of tracer present in the tumor[13]. We demonstrate feasibility for human-scale tumor imaging with ferumoxytol by imaging a glioblastoma phantom filled with tracer at 0.06% of the approved dose[30] (**Extended Data Figure 8a**). MPI may also find use in monitoring interventional procedures[21,44], without the limitations of radiation dose and tracer toxicity, such as transarterial embolization procedures and angiography, traditionally performed using X-ray-based technologies including fluorscopy and X-ray CT. To model these interventional procedures, we performed real-time imaging of an arterial phantom filling with tracer, and static, tomographic imaging of an anigiography phantom (**Extended Data Figure 8b,c**, **Supplemental Video SV2**). MPI can also address new applications such as monitoring cell therapies[7–12] or imaging metastasis-associated inflammation[13,14], especially paired with the ongoing development of magnetic tracers designed with application-specific coatings and improved MPI performance[52,53]. Recent work has also shown MPI can detect the magnetic signal from hemosiderin, an endogenous hemoglobin degradation product, and was demonstrated as a high-contrast biomarker for unstable plaques by imaging intraplaque hemorrhage in human endoarterectomy samples and an *in vivo* animal model[22].

In this work, we report the first-in-human imaging with MPI in healthy subjects and establish the clinical feasibility of this technology. MPI introduces a unique imaging physics principle to tomographic medical imaging, comparable to the introduction of clinical gamma camera, PET, Ultrasound, MRI, and CT. Until now, MPI capabilities had only been demonstrated in small animals but lacked a pathway to testing in humans. This work demonstrates that pathway, enabling the exploration of MPI across a broad range of

clinical applications, and providing a foundation for future studies in patients.

Author Contributions

E.E.M. and O.C.S. contributed equally to this work and share first authorship. P.W.G., A.M.L., S.Y.L., E.M.P. and M.W. conceptualized the original idea for the research. B.D., E.M., E.E.M., K.F., E.B. and P.W.G. designed and constructed the imager hardware. J.J.K. and E.B. designed and developed the system software. T.S. developed the image reconstruction algorithm. J.J.K., T.S., and E.E.M. contributed to data processing software. E.E.M., O.C.S., T.S. and E.M. ran formal data analyses. M.G.W., O.C.S., E.E.M., B.D., J.J.K., E.M., A.M.L., S.Y.L., M.W. and P.W.G. contributed to the clinical study design. B.D., M.G.W., A.R.M., J.J.K., E.E.M. and E.B. verified the imager hardware and software for study use. M.G.W. administered the clinical study. M.G.W., O.C.S., B.D., E.E.M., A.R.M., E.M.P. and A.M.L. conducted the clinical study. M.G.W., E.E.M., B.D., J.J.K. and O.C.S. managed the study data curation. E.E.M., O.C.S., B.D., E.M. and A.R.M. produced the phantom MPI studies. O.M., O.C.S. and M.W. performed the phantom nuclear studies. O.C.S., N.F. and P.J.F. ran the preclinical mouse studies. A.M.L., S.Y.L., E.M.P. and M.W. provided clinical feedback and guidance. C.A.R. and P.W.G. supervised and provided funding for the project. P.W.G., O.C.S. and E.E.M. wrote the initial draft of the manuscript. E.E.M., O.C.S., P.W.G., K.F. and E.M. produced the data visualizations. C.M.R.-R., M.G.W., M.W., and T.S. contributed to substantial editing of the manuscript. All authors reviewed and approved the manuscript.

Acknowledgements

The authors thank Walter Fetsch, Mike Chandeeing, David Trease, Ashley Truxal, and John Carl for contributions to the design, construction, and documentation of the imager; Jonthan Lucero, Carlos Carrero, Juan Carrero, and Yessenia Aguilar for their onsite manufacturing and facilities support; Joan Greve for protocol development and benchmarking against MRI standards during the preliminary phases of this project; Benjamin Fellows for early contributions to study documentation; and Vanessa Eriksson and Myhanh Bui for administrative assistance. We gratefully acknowledge venture capital funding from 5AM Ventures and Celesta Capital. Research reported in this publication was also supported in part by the National Institute of Biomedical Imaging and Bioengineering and the National Cancer Institute of the National Institutes of Health under award numbers R44EB029877, R44EB035078, R44EB020463, R44DA041814, R44CA285064, and R01CA298804. The content is solely the responsibility of the authors and does not necessarily represent the official views of the National Institutes of Health.

Data Availability

Participant demographics, imaging parameters, and longitudinal model results are provided in the Article and Supplementary Information. Two anonymized MPI imaging datasets corresponding to Fig. 1 are provided in 3D Slicer-compatible format as Supplementary Data.

Code Availability

As detailed in Methods, image quantitation and analyses were performed using standard methodologies; no code implementing novel analytical algorithms central to the main findings was developed. Image reconstruction used a previously published algorithm, described and cited in Methods.

References

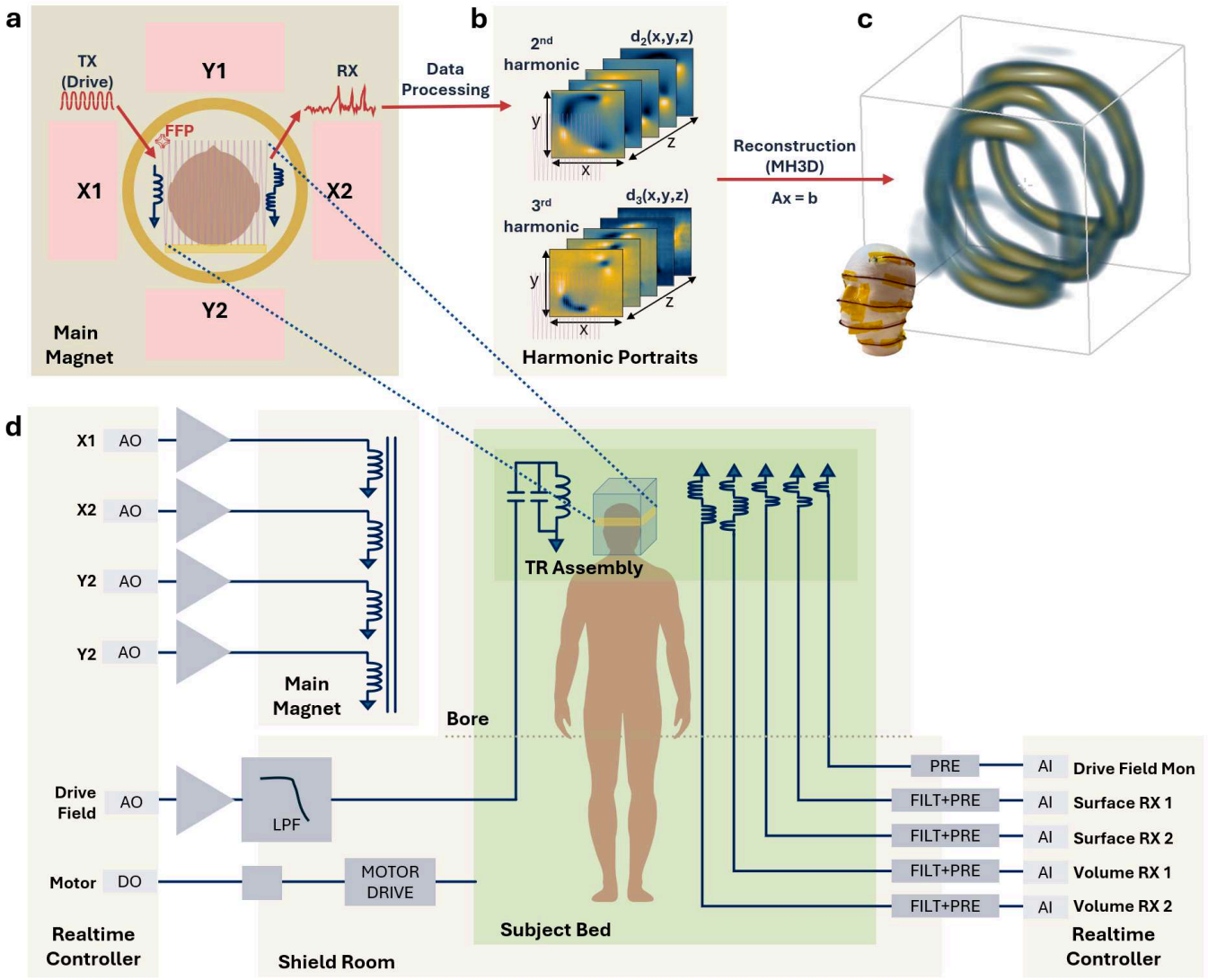
1. Saritas, E. U. *et al.* Magnetic particle imaging (MPI) for NMR and MRI researchers. *Journal of Magnetic Resonance* **229,** 116–126. ISSN: 10907807 (Apr. 2013).
2. Rivera-Rodriguez, A. & Rinaldi-Ramos, C. M. Emerging Biomedical Applications Based on the Response of Magnetic Nanoparticles to Time-Varying Magnetic Fields. *Annu. Rev. Chem. Biomol. Eng. 2021* **12,** 163–185 (2021).
3. Sehl, O. C. *et al.* Magnetic particle imaging enables nonradioactive quantitative sentinel lymph node identification: feasibility proof in murine models. *Radiology Advances* **1.** ISSN: 2976-9337 (Sept. 2024).
4. Thompson, J. F. *et al.* Same-day or next-day sentinel node biopsy after lymphoscintigraphy for melanoma using 99m Tc-labelled antimony sulphide colloid. *The British journal of surgery* **107,** 1773–1779. ISSN: 1365-2168. https://pubmed.ncbi.nlm.nih.gov/32820818/ (Dec. 2020).
5. Moncayo, V. M., Grady, E. E., Alazraki, N. P. & Aarsvold, J. N. Sentinel-Lymph-Node Multicenter Trials. *Seminars in Nuclear Medicine* **50,** 56–74. ISSN: 15584623 (Jan. 2020).
6. Alazraki, N., Glass, E. C., Castronovo, F., Olmos, R. A. V. & Podoloff, D. Procedure Guideline for Lymphoscintigraphy and the Use of Intraoperative Gamma Probe for Sentinel Lymph Node Localization in Melanoma of Intermediate Thickness 1.0*. *The Journal of Nuclear Medicine* **43** (2002).
7. Rivera-Rodriguez, A. *et al.* Tracking adoptive T cell immunotherapy using magnetic particle imaging. *Nanotheranostics* **5,** 431–444. ISSN: 22067418 (2021).
8. Wu, W. E. *et al.* Multimodal in Vivo Tracking of Chimeric Antigen Receptor T Cells in Preclinical Glioblastoma Models. *Investigative Radiology* **58,** 388–395. ISSN: 15360210 (June 2023).
9. Sehl, O. C. *et al.* Preclinical and Clinical-Scale Magnetic Particle Imaging of Natural Killer Cells: in vitro and ex vivo Demonstration of Cellular Sensitivity, Resolution, and Quantification. *Molecular Imaging and Biology.* ISSN: 1536-1632 (Dec. 2024).
10. Fink, C. *et al.* In vivo tracking of adenoviral-transduced iron oxide-labeled bone marrow-derived dendritic cells using magnetic particle imaging. *European Radiology Experimental* **7.** ISSN: 25099280 (Dec. 2023).
11. Bulte, J. W. M. *et al.* Quantitative "Hot-Spot" Imaging of Transplanted Stem Cells Using Superparamagnetic Tracers and Magnetic Particle Imaging. *Tomography* **1,** 91–97 (Dec. 2015).
12. Zheng, B. *et al.* Quantitative magnetic particle imaging monitors the transplantation, biodistribution, and clearance of stem cells in vivo. *Theranostics* **6,** 291–301. ISSN: 18387640 (2016).
13. Makela, A. V. *et al.* Magnetic Particle Imaging of Macrophages Associated with Cancer: Filling the Voids Left by Iron-Based Magnetic Resonance Imaging. *Molecular Imaging and Biology* **22,** 958–968. ISSN: 18602002 (Aug. 2020).
14. Korangath, P. *et al.* Nanoparticle Retention Enables Non-invasive Detection of Metastases by Magnetic Particle Imaging in Murine Breast Cancer Models. *Nanotheranostics* (2025).
15. Peng, Z. *et al.* Sensitive and quantitative in vivo analysis of PD-L1 using magnetic particle imaging and imaging-guided immunotherapy. *European Journal of Nuclear Medicine and Molecular Imaging* **50,** 1291–1305. ISSN: 1619-7070. https://link.springer.com/10.1007/s00259-022-06083-2 (Apr. 2023).
16. Tay, Z. W. *et al.* Magnetic Particle Imaging-Guided Heating in Vivo Using Gradient Fields for Arbitrary Localization of Magnetic Hyperthermia Therapy. *ACS Nano* **12,** 3699–3713. ISSN: 1936086X (Apr. 2018).
17. Healy, S. *et al.* Clinical magnetic hyperthermia requires integrated magnetic particle imaging. *Wiley Interdisciplinary Reviews: Nanomedicine and Nanobiotechnology* **14,** e1779. ISSN: 1939-0041. https://onlinelibrary.wiley.com/doi/full/10.1002/wnan.1779 (May 2022).

18. Mason, E. E. *et al.* Functional magnetic particle imaging (fMPI) of cerebrovascular changes in the rat brain during hypercapnia. *Physics in Medicine and Biology* **68.** ISSN: 13616560 (Sept. 2023).
19. Wei, Z. *et al.* First Nonhuman Primate-Sized Magnetic Particle Imaging System Based on Digital-Scanned Focus Field. *IEEE Transactions on Instrumentation and Measurement* **73.** ISSN: 15579662 (2024).
20. Barksdale, A. C. *et al.* Measurement of cerebral blood volume modulation in non-human primates. *International Journal on Magnetic Particle Imaging* **11.** ISSN: 23659033 (2025).
21. Hartung, V. *et al.* Magnetic particle imaging angiography of the femoral artery in a human cadaveric perfusion model. *Communications Medicine* **5,** 1–10. ISSN: 2730664X. https://www.nature.com/articles/s43856-025-00794-x (Dec. 2025).
22. Tong, W. *et al.* Highly sensitive magnetic particle imaging of vulnerable atherosclerotic plaque with active myeloperoxidase-targeted nanoparticles. *Theranostics* **11,** 506–521. ISSN: 1838-7640 (2021).
23. Gleich, B. & Weizenecker, J. Tomographic imaging using the nonlinear response of magnetic particles. *Nature* **435,** 1214–1217. ISSN: 1476-4687. https://doi.org/10.1038/nature03808 (2005).
24. Dames Andrew, N. *Spatial Magnetic Interrogation. Patent WO96/31790* Apr. 1996.
25. Goodwill, P. W. & Conolly, S. M. Multidimensional X-Space Magnetic Particle Imaging. *IEEE Transactions on Medical Imaging* **30,** 1581–1590. ISSN: 0278-0062. http://ieeexplore.ieee.org/document/5728922/ (Sept. 2011).
26. Lu, K., Goodwill, P. W., Saritas, E. U., Zheng, B. & Conolly, S. M. Linearity and Shift Invariance for Quantitative Magnetic Particle Imaging. *IEEE Transactions on Medical Imaging* **32,** 1565–1575. ISSN: 0278-0062. http://ieeexplore.ieee.org/document/6494648/ (Sept. 2013).
27. Keselman, P. *et al.* Tracking short-term biodistribution and long-term clearance of SPIO tracers in magnetic particle imaging. *Physics in Medicine and Biology* **62,** 3440–3453. ISSN: 13616560 (Apr. 2017).
28. Ahlborg, M., Buzug, T. M. & Wegner, F. 20 years of magnetic particle imaging – from patents to patients. *Biochemical and Biophysical Research Communications* **781.** ISSN: 10902104 (Sept. 2025).
29. AMAG Pharmaceuticals. *Feraheme (ferumoxytol injection) Prescribing Information* June 2022. https://www.accessdata.fda.gov/drugsatfda_docs/label/2022/022180s025lbl.pdf.
30. Azurity Pharmaceuticals. *Ferabright (ferumoxytol injection) Prescribing Information* Oct. 2025. https://www.accessdata.fda.gov/drugsatfda_docs/label/2025/219868s000lbl.pdf.
31. Grégoire, V. *et al.* Delineation of the neck node levels for head and neck tumors: A 2013 update. DAHANCA, EORTC, HKNPCSG, NCIC CTG, NCRI, RTOG, TROG consensus guidelines. *Radiotherapy and Oncology* **110,** 172–181. ISSN: 18790887 (2014).
32. Leong, S. P. Detection of melanoma, breast cancer and head and neck squamous cell cancer sentinel lymph nodes by Tc-99m Tilmanocept (Lymphoseek®). *Clinical & Experimental Metastasis* **39,** 39–50. ISSN: 0262-0898 (Feb. 2022).
33. Cadena-Pineros, E., Goìmez-Herrera, J., Mayo-Patiño, M. & Carreño, A. Advantages of sentinel lymph node mapping by single photon emission computed tomography/computed tomography in early-stage malignant head-and-neck skin tumors. *Indian Journal of Nuclear Medicine* **37,** 43–49. ISSN: 09740244 (Jan. 2022).
34. Aldenhoven, L. *et al.* Sentinel lymph node mapping with superparamagnetic iron oxide for melanoma: a pilot study in healthy participants to establish an optimal MRI workflow protocol. *BMC cancer* **22.** ISSN: 1471-2407. https://pubmed.ncbi.nlm.nih.gov/36241982/ (Dec. 2022).
35. Endomagnetics Ltd. *Summary of Safety and Effectiveness Data: Magtrace® and Sentimag® Magnetic Localization System* tech. rep. (Dec. 2022).

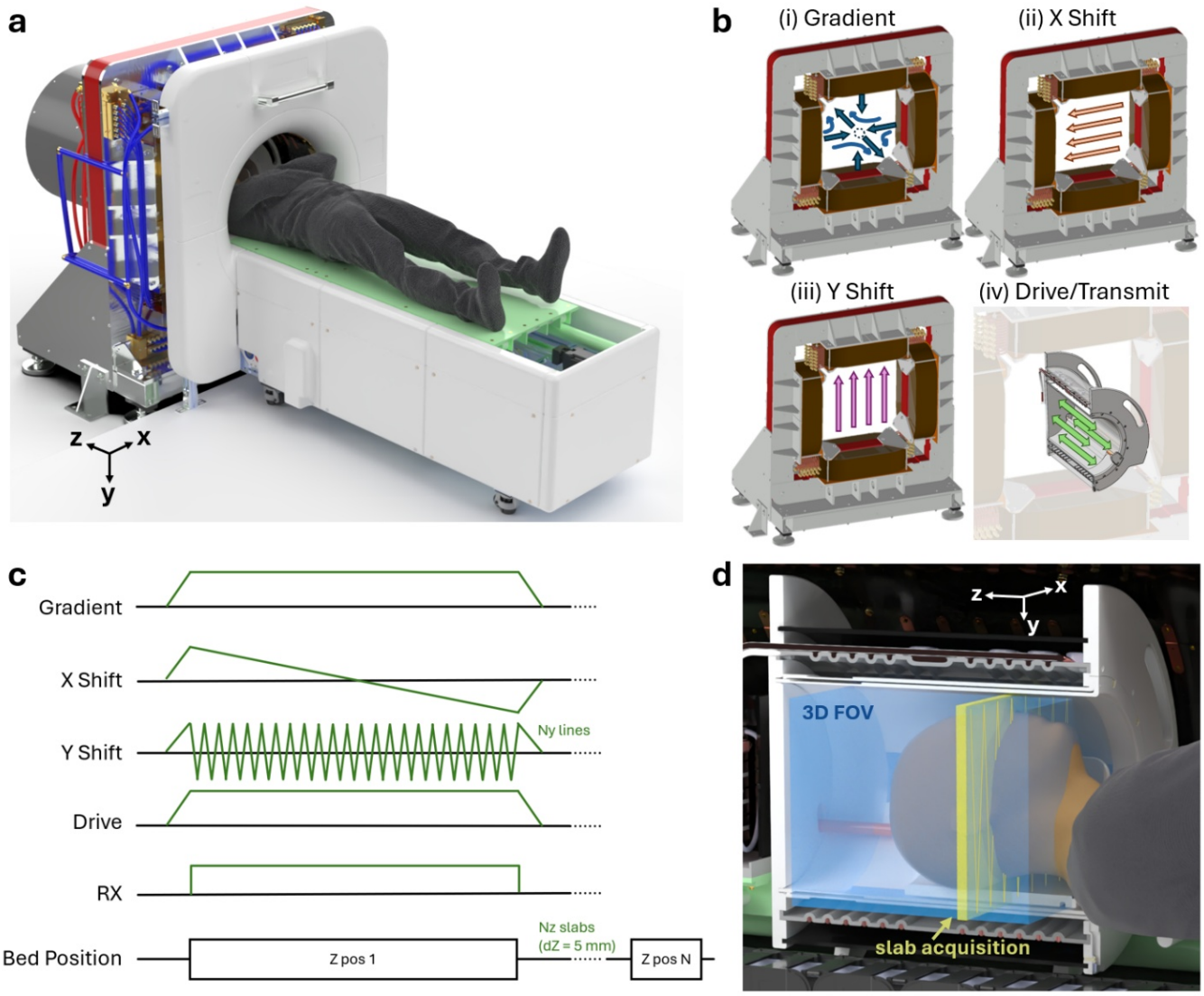
36. Pedro, L., Harmer, Q., Mayes, E. & Shields, J. D. Impact of Locally Administered Carboxydextran-Coated Super-Paramagnetic Iron Nanoparticles on Cellular Immune Function. *Small* **15.** ISSN: 16136829 (May 2019).
37. Harrell, M. I., Iritani, B. M. & Ruddell, A. Lymph node mapping in the mouse. *Journal of Immunological Methods* **332,** 170–174. ISSN: 00221759 (Mar. 2008).
38. Bulte, J. W. Superparamagnetic iron oxides as MPI tracers: A primer and review of early applications. *Advanced Drug Delivery Reviews* **138,** 293–301. ISSN: 18728294 (Jan. 2019).
39. Graeser, M. *et al.* Human-sized magnetic particle imaging for brain applications. *Nature Communications* **10,** 1936. ISSN: 2041-1723 (Dec. 2019).
40. Rahmer, J., Stehning, C. & Gleich, B. Remote magnetic actuation using a clinical scale system. *PLOS ONE* **13,** e0193546. ISSN: 1932-6203. https://journals.plos.org/plosone/article?id=10.1371/journal.pone.0193546 (Mar. 2018).
41. Mattingly, E. *et al.* Design, construction and validation of a magnetic particle imaging (MPI) system for human brain imaging. *Physics in Medicine & Biology* **70,** 015019. ISSN: 0031-9155. https://pubmed.ncbi.nlm.nih.gov/39662051/ (Jan. 2025).
42. Le, T. A. *et al.* Towards human-scale magnetic particle imaging: development of the first system with superconductor-based selection coils. *IEEE Transactions on Medical Imaging*. ISSN: 1558254X (2024).
43. Nomura, K. *et al.* Development of human head size magnetic particle imaging system. *International Journal on Magnetic Particle Imaging* **10.** ISSN: 23659033 (2024).
44. Vogel, P. *et al.* iMPI: portable human-sized magnetic particle imaging scanner for real-time endovascular interventions. *Scientific reports* **13,** 10472. ISSN: 2045-2322 (June 2023).
45. Douek, M. *et al.* Sentinel Node Biopsy Using a Magnetic Tracer Versus Standard Technique: The SentiMAG Multicentre Trial. *Annals of Surgical Oncology* **21,** 1237–1245. ISSN: 1068-9265 (Apr. 2014).
46. Karakatsanis, A. *et al.* Delayed Sentinel Lymph Node Dissection in Patients with a Preoperative Diagnosis of Ductal Cancer In Situ by Preoperative Injection with Superparamagnetic Iron Oxide (SPIO) Nanoparticles: The SentiNot Study. *Annals of Surgical Oncology* **30,** 4064–4072. ISSN: 1068-9265 (July 2023).
47. Taruno, K. *et al.* Multicenter clinical trial on sentinel lymph node biopsy using superparamagnetic iron oxide nanoparticles and a novel handheld magnetic probe. *Journal of Surgical Oncology* **120,** 1391–1396. ISSN: 0022-4790. https://onlinelibrary.wiley.com/doi/10.1002/jso.25747 (Dec. 2019).
48. Cardinal Health. *Lymphoseek (technetium Tc 99m tilmanocept) Prescribing Information* May 2021. https://www.accessdata.fda.gov/drugsatfda_docs/label/2021/202207s012lbl.pdf.
49. Sekino, M. *et al.* Handheld magnetic probe with permanent magnet and Hall sensor for identifying sentinel lymph nodes in breast cancer patients. *Scientific Reports* **8.** ISSN: 20452322 (Dec. 2018).
50. International Atomic Energy Agency. *Radiopharmaceuticals for sentinel lymph node detection: status and trends* tech. rep. (Vienna, Apr. 2015). https://www-pub.iaea.org/MTCD/Publications/PDF/Pub1674web-3264500.pdf.
51. Nieuwenhuis, E. R. *et al.* A complete magnetic sentinel lymph node biopsy procedure in oral cancer patients: A pilot study. *Oral Oncology* **121,** 105464. ISSN: 13688375 (Oct. 2021).
52. Tay, Z. W. *et al.* Superferromagnetic Nanoparticles Enable Order-of-Magnitude Resolution & Sensitivity Gain in Magnetic Particle Imaging. *Small Methods* **5,** 2100796. ISSN: 2366-9608. https://onlinelibrary.wiley.com/doi/10.1002/smtd.202100796 (Nov. 2021).
53. Velazquez-Albino, A. C., Daniel Imhoff, E. & Rinaldi-Ramos, C. M. Advances in engineering nanoparticles for magnetic particle imaging (MPI). *Sci. Adv* **11,** 7356. https://www.science.org (2025).

54. West, G. B., Brown, J. H. & Enquist, B. J. A General Model for the Origin of Allometric Scaling Laws in Biology. *Science* **276,** 122–126. ISSN: 0036-8075. https://www.science.org/doi/10.1126/science.276.5309.122 (Apr. 1997).
55. Shinaoka, A. *et al.* Lower-Limb Lymphatic Drainage Pathways and Lymph Nodes: A CT Lymphangiography Cadaver Study. *Radiology* **294,** 223–229. ISSN: 1527-1315. https://pubmed.ncbi.nlm.nih.gov/31746690/ (2020).

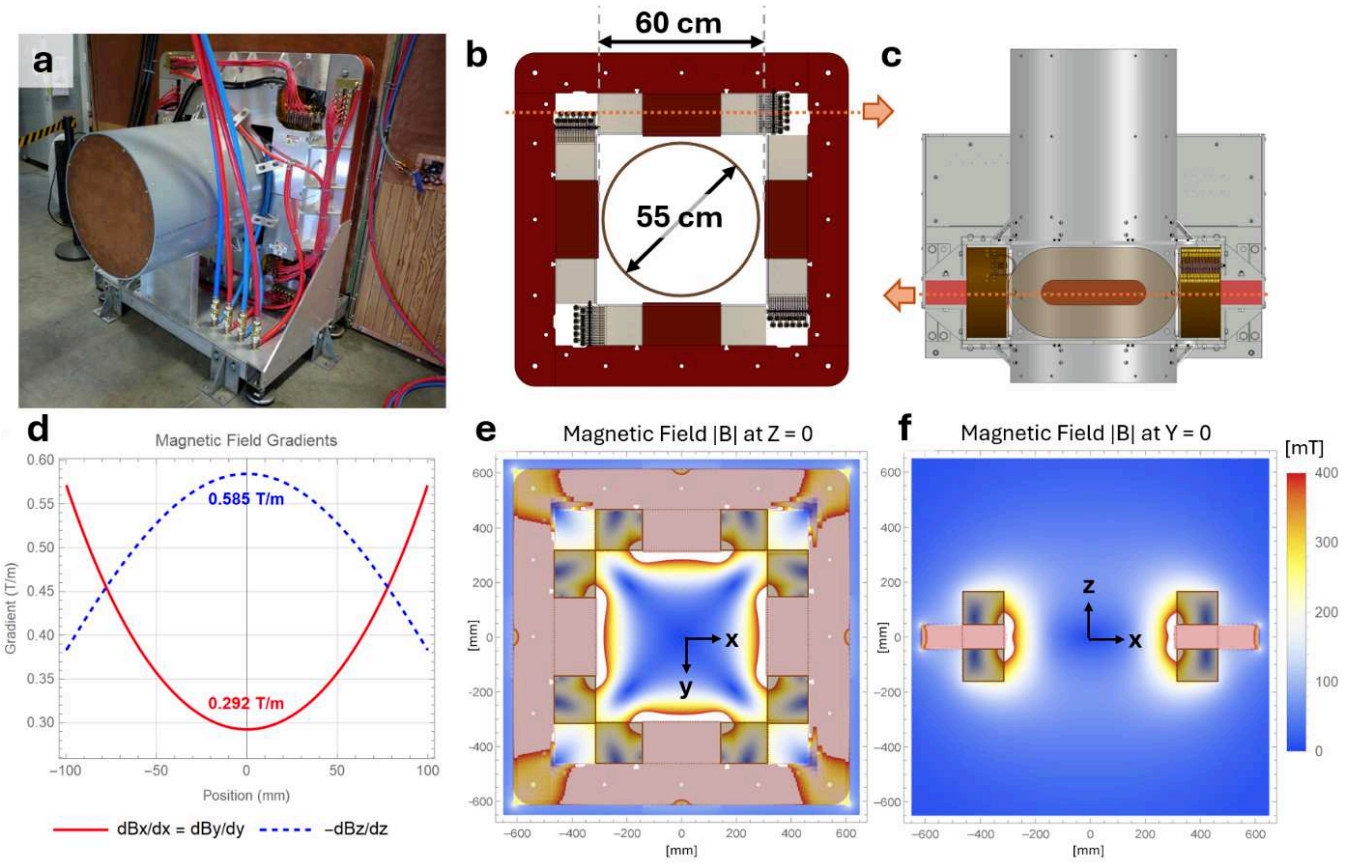
Extended Data



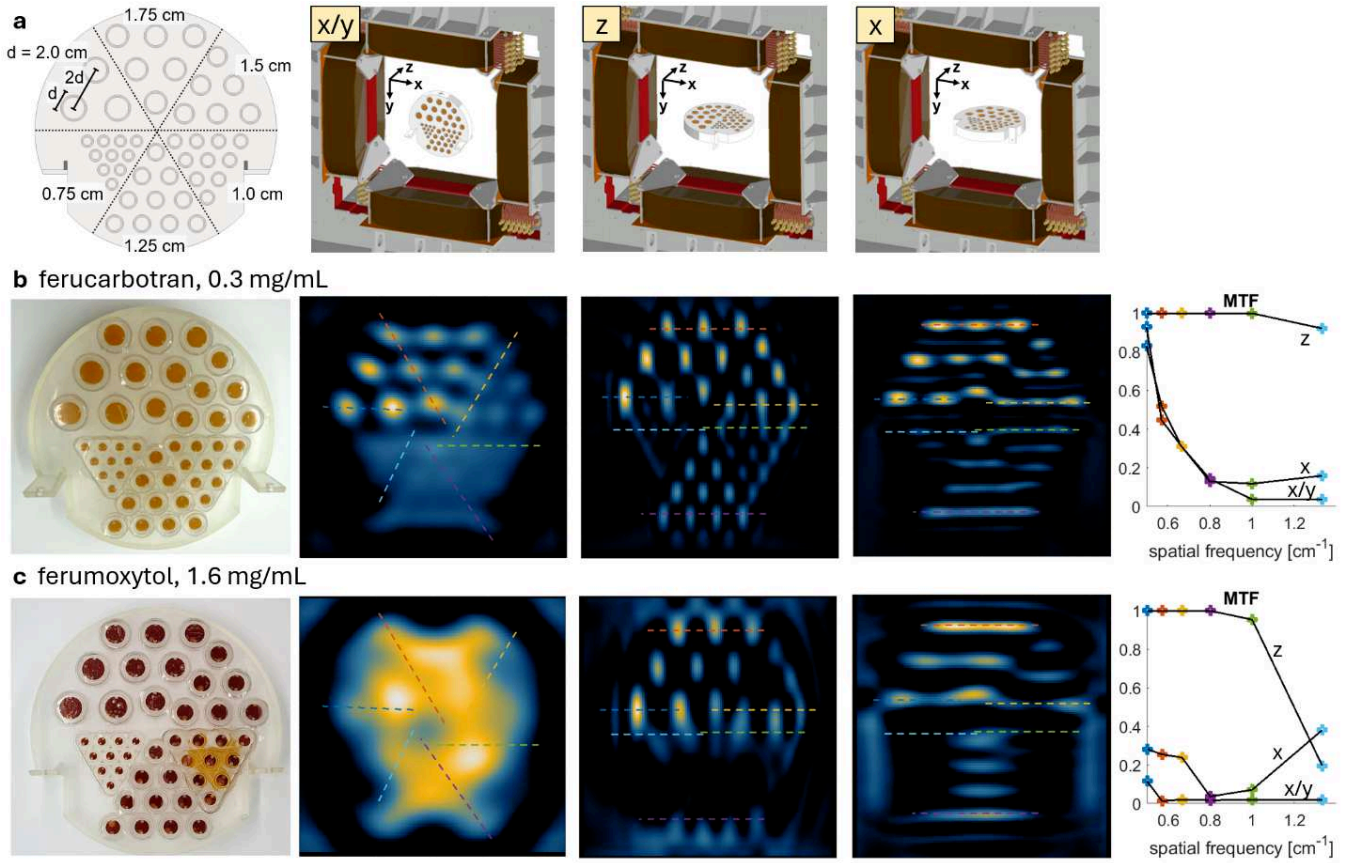
Extended Data Figure 1: MPI image formation and system diagram. (a) To sample MPI signal over a volume of interest, the selection field (here a field free point, FFP) is generated and scanned across the sample by the main magnet (consisting of coils X1, X2, Y1, Y2), while the time-varying drive field (TX) induces the nonlinear magnetization of the tracer particles, whose signal is picked up inductively as voltage in receiver coils (RX). **(b)** The data is processed into an intermediate data format known as 'harmonic portraits' ($d_k(x,y,z)$, k=2,3...) for each received signal, at each z position of the patient bed. **(c)** The MH3D reconstruction (see **Methods**) implements a multi-frame deconvolution of the harmonic portraits to form a 3D image of the tracer distribution. **(d)** A simplified system diagram illustrating control and signal flow starting with the real-time controller of the main magnet, drive, and bed motor. The magnetic fields produced by the main magnet and drive coil interact with the magnetic tracer in the field of view, with active control of the drive field amplitude and phase (Drive Field Mon). The magnetic tracer signal is then received, filtered, amplified, and digitized by the same real-time controller.



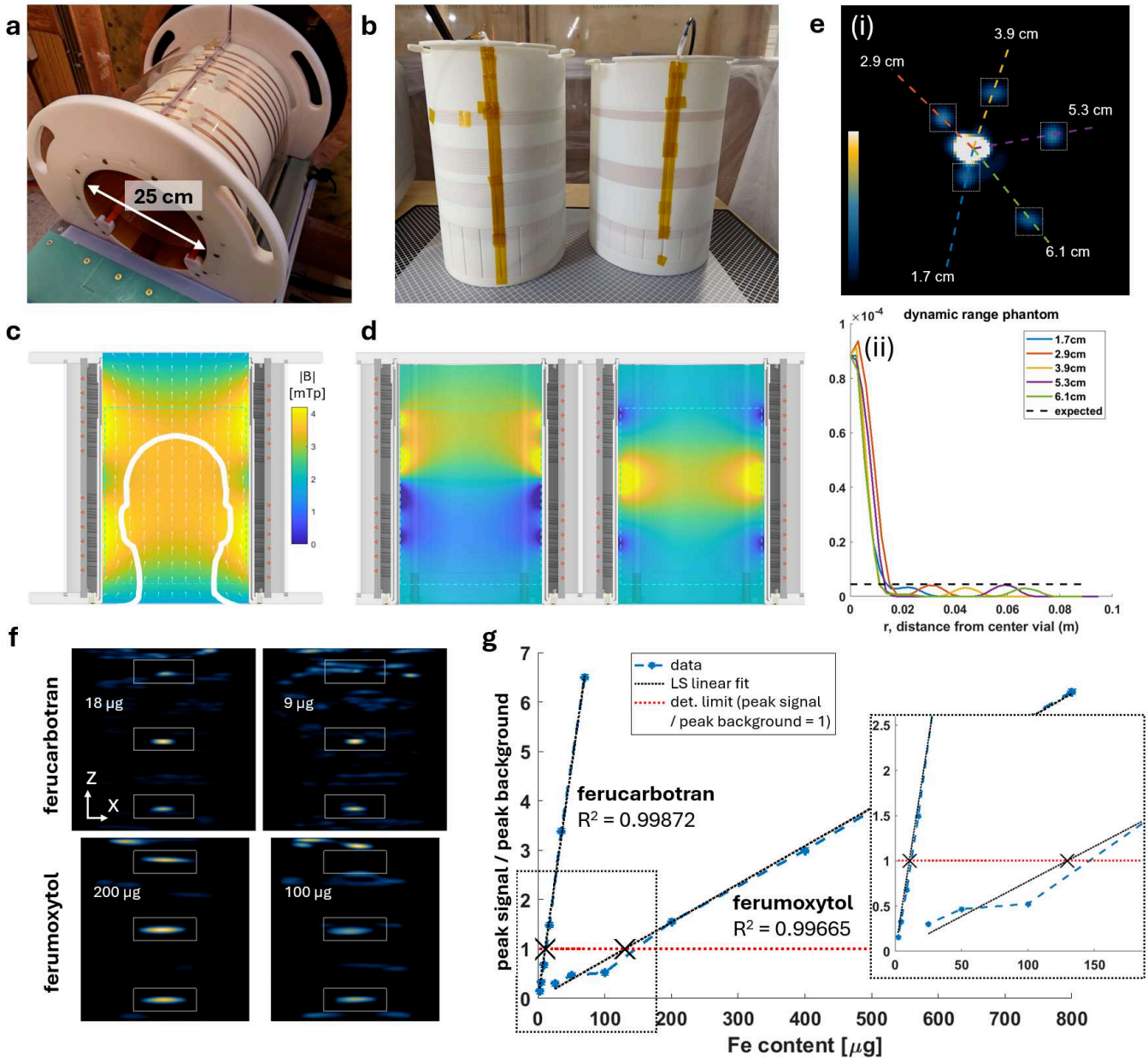
Extended Data Figure 2: Overview of human MPI hardware and imaging sequence. **(a)** A CAD rendering of the MPI imager shown without shield room walls illustrates the main magnet structure, bore tube, patient bed, and a representative position of the subject during imaging, with their head inside the imaging bore. **(b)** Each of the applied magnetic fields is illustrated: the gradient, Y shift, X shift, all produced by the main magnet, and drive (transmit) field. **(c)** A representative pulse sequence is used to acquire data from a slab, which is repeated at Nz bed positions to image the full FOV. **(d)** A CAD rendering cross-section shows the human head positioned within the transmit/receive assembly, with the slab acquisition from (c) represented in yellow, and the maximum FOV (24 × 24 × 30 cm) in blue. This example pulse sequence (c,d) scans the field free point in the xy plane using a triangular shift waveform with fast shift y and slow shift x. The drive field rapidly moves the field free point in z, defining the slab thickness. The subject bed is stepped along z to acquire multiple overlapping slabs, enabling the full axial FOV coverage.



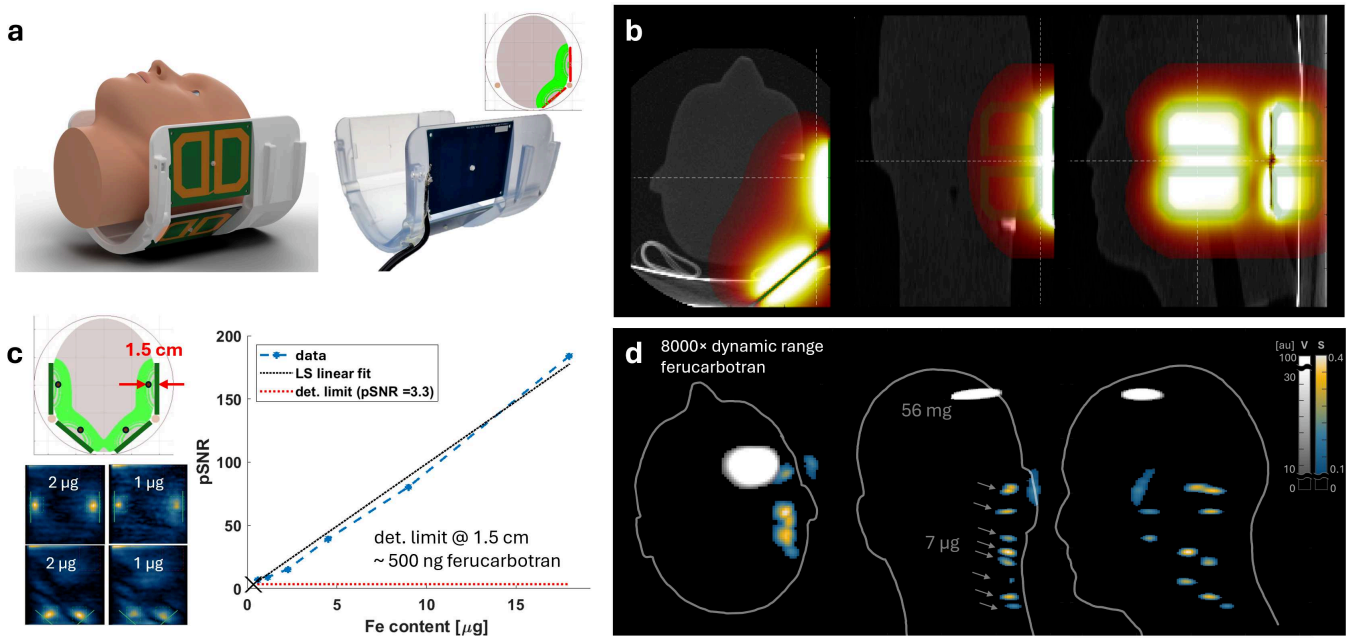
Extended Data Figure 3: Main magnet assembly detail. **(a)** Close-up of main magnet assembly with the water-cooling (blue and red hoses) visible. **(b)** Axial cross-section through the magnet isocenter and **(c)** coronal cross-section through the top electromagnet show the coil and yoke configuration, highlighting the 60 cm main magnet bore and 55 cm free bore. Orange dotted lines in (b) and (c) show corresponding cross-section locations. **(d)** Simulated magnetic field gradients at isocenter. **(e)** A simulated magnetic field map shows the fields present in the iron yoke and free bore in axial (z = 0) and **(f)** coronal (y = 0) views.



Extended Data Figure 4: Measured modulation transfer function (MTF) resolution using a Derenzo phantom filled with ferucarbotran and ferumoxytol at a gradient strength of dBx × dBy × dBz = 0.3 × 0.3 × 0.6 T/m. Data points used in the MTF calculation are illustrated as line ROIs overlaid on the 2D slices. **(a)** The phantom was 3D printed and had well sizes ranging from 0.75 cm to 2.00 cm, with 0.70 cm depth. Tomographic volumes were acquired for multiple phantom orientations to capture the anisotropic imager resolution. **(b)** Ferucarbotran resolution was measured to be 1-1.25 cm in x/y (20% MTF) and 0.75 cm in z (90% MTF). **(c)** Ferumoxytol resolution was measured to be >2 cm in x/y and 1.25 cm in z (20% MTF). The leakage seen in the 1.0 cm wells does not impact the results since it is below the resolvable resolution of the tracer.



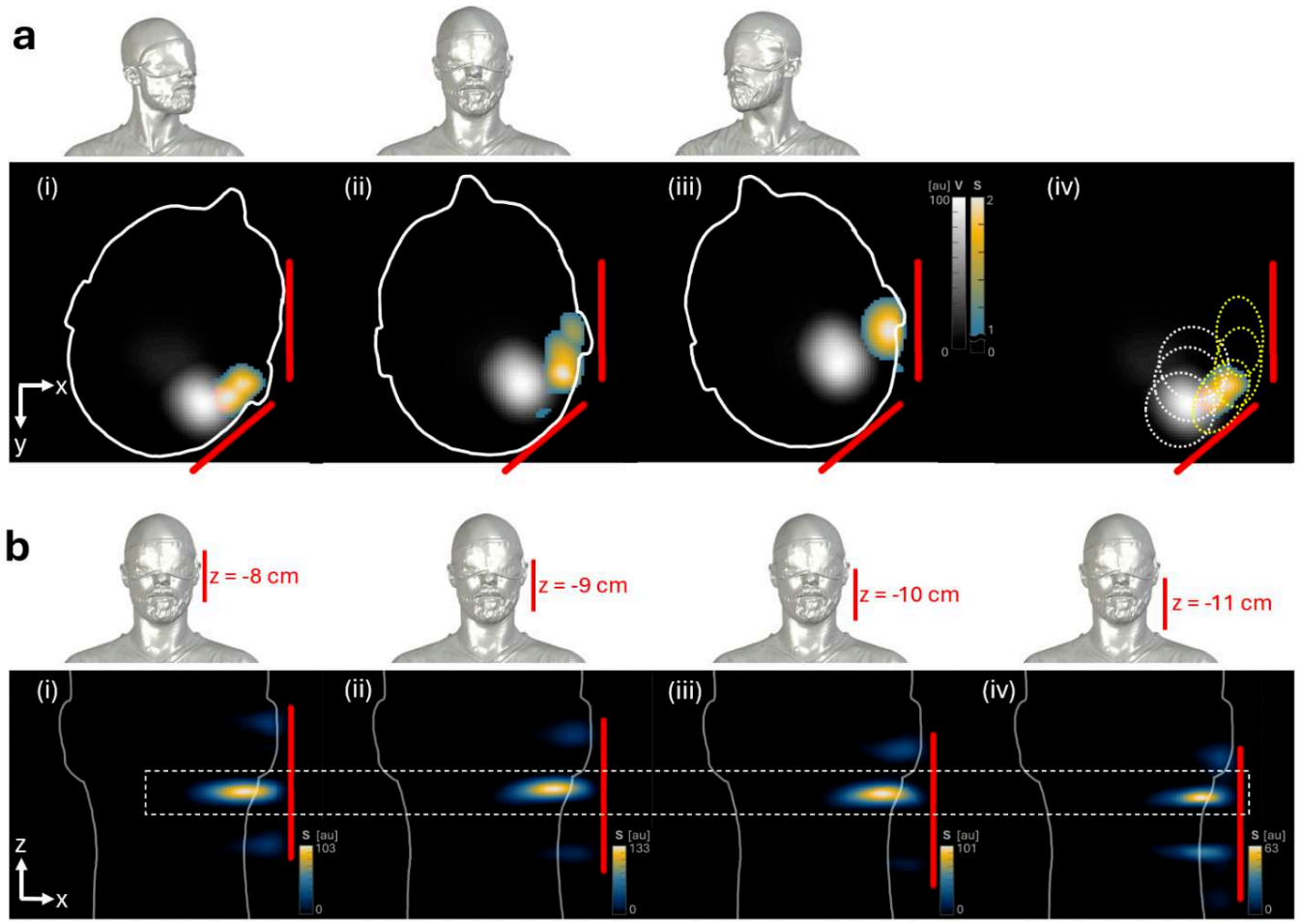
Extended Data Figure 5: Performance characterization of a head-and-neck volume transmit/receive (T/R) coil assembly. (a) Photo of the as-built T/R assembly showing the solenoidal transmit windings and the 25 cm imaging free bore. **(b)** Photo of the two volume receive coils that are mounted concentrically inside the transmit coil in (a). **(c)** Sagittal cross-section of the T/R assembly showing the drive magnetic field magnitude (|B|), and **(d)** the two volume receive coils' sensitivity maps (B_z component). **(e)** (i,ii) MPI of a shine-through phantom comprised of a central sample containing 2.8 mg Fe surrounded by 5 samples containing 140 µg Fe, demonstrating >20× dynamic range at distances of 1.7–6.1 cm in X/Y plane. The tracer quantities were selected to match phantom studies performed using handheld magnetic probes (see **Methods**). **(f)** Sensitivity measured using a dilution series estimates **(g)** detection limits of ~10 µg for ferucarbotran and ~130 µg for ferumoxytol. The MPI signal was linear with tracer quantity (ferucarbotran $R^2 = 0.999$, ferumoxytol $R^2 = 0.997$).



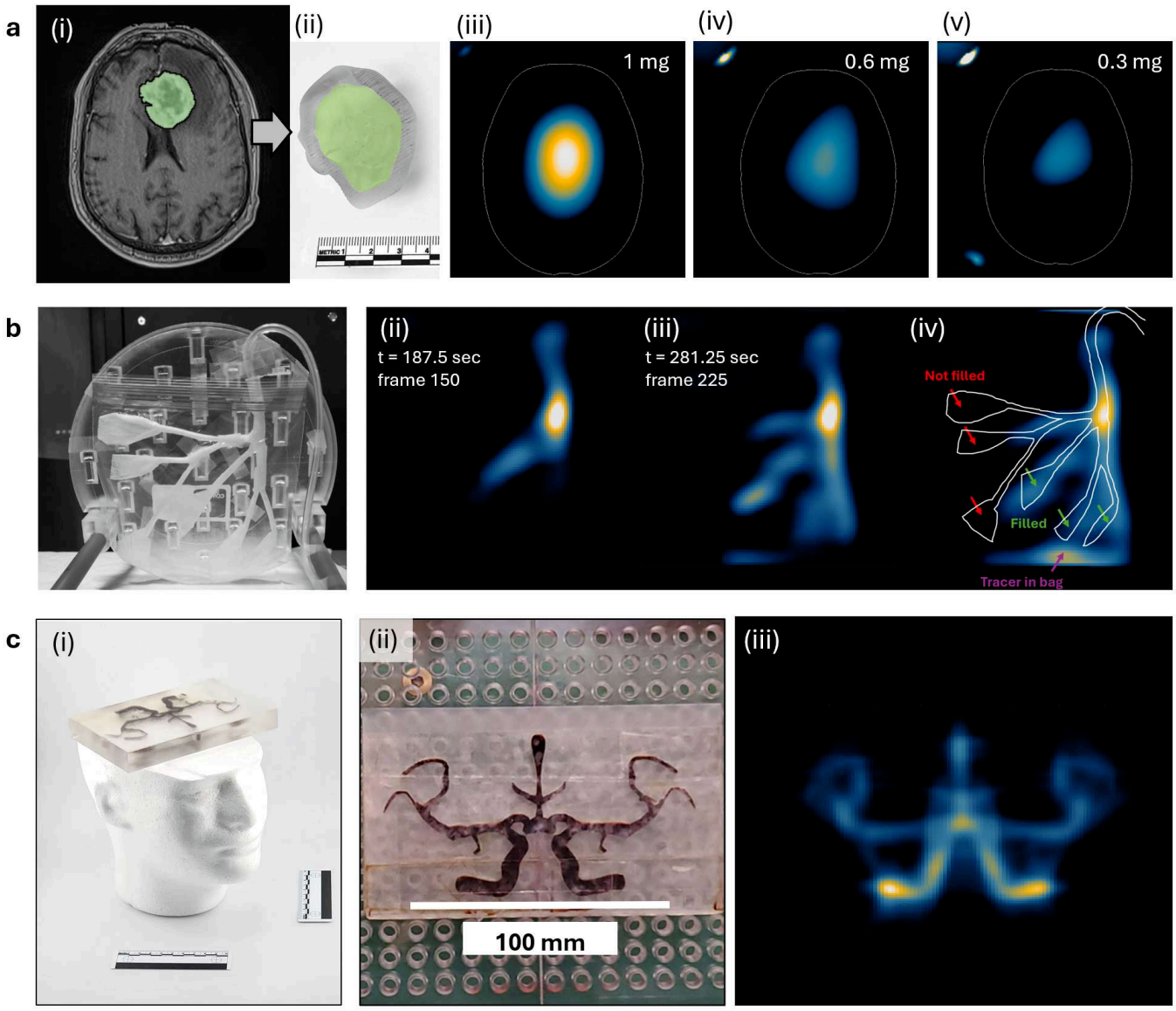
Extended Data Figure 6: Design, construction, and characterization of an application-specific surface coil array designed to improve sensitivity and shine-through performance. The surface coil array can be configured in left, right, or bilateral configurations. **(a)** Render and photograph of the array in its left-side configuration. **(b)** Contour maps show the left-side configuration field maps in axial, coronal, and sagittal views overlaid on an X-ray CT. **(c)** A dilution series sensitivity assessment of the surface coils is performed using the bilateral configuration, showing a detection limit of ~500 ng ferucarbotran at a distance of ~1.5 cm from the coil surface. **(d)** To test shine-through performance, we imaged a lymph node phantom (see **Figure 4**) filled with ferucarbotran at an 8000:1 ratio in tracer quantity between mock injection site (56 mg Fe) and mock lymph nodes (11×, 7 µg Fe each) and found that 10 of 11 mock nodes were resolvable. MPI axial, coronal and sagittal MIPs are displayed using two colormaps with volume coils displayed in grayscale and surface coils in color.

Extended Data Table 1: System specifications and measured performance.

Parameter	Measured Performance	Notes
Magnet bore diameter	60 cm	Pole piece to pole piece
Patient bore diameter	55 cm	Inside copper shield, accommodates shoulders
Imaging free bore diameter	25 cm	ID of volume receive coils, accommodates heads
Gradient strength	0.3 × 0.3 × 0.6 T/m (x,y,z)	
FOV	24 × 24 × 30 cm (x,y,z)	FOVxy is covered using electromagnet shift fields, FOVz is covered using mechanical translation of the bed
Drive frequency	45.01 kHz	
Drive amplitude	$\leq$ 3.5 mT peak	
Detection limit, volume coils	10 μg Fe (ferucarbotran) 130 μg Fe (ferumoxytol)	Sensitivity is approximately constant within the FOV
Detection limit, surface coils	500 ng Fe @ 1.5 cm distance (ferucarbotran)	Sensitivity changes with distance from the coil
Resolution, ferucarbotran	1-1.25 cm in x/y (20% MTF) est. 0.3 cm in z (20% MTF)	z resolution is estimated as the phantom did not test below 0.75 cm in z (90% measured MTF)
Resolution, ferumoxytol	est. >2 cm in x/y 1.25 cm in Z (20% MTF)	x,y resolution visually estimated as the phantom did not test above 2 cm
Dynamic range / shine-through	Demonstrated 8000:1 with surface coils	When using surface coils, coil positioning drives shine-through performance



Extended Data Figure 7: Confirmation of signal in lymph node regions. (a) In a first test to confirm that the signals at the lymph node regions maintain a consistent anatomical position within a subject's head anatomy, a series of images (i, ii, iii) were acquired while the subject rotated their head through three positions. MPI axial MIPs from the crown through the laryngeal prominence are displayed. MPI signal detected from volume coils (V) shows the injection site and is displayed in grayscale. MPI signal from surface coils (S) show the lymph node regions displayed in color. The red lines indicate the position of the surface coils. (iv) The localization of the injection site and lymphatic signals at all three subject positions are summarized with dotted circles, showing the rotation of the MPI signals following the subject anatomy. **(b)** In a second test, a series of images were acquired while the surface coils were adjusted to four positions (i, ii, iii, iv) along the superior-inferior axis of the subject head while the subject position was maintained. MPI coronal MIPs are displayed. In each image, MPI signal was detected in the same cervical lymph node region despite repositioning of the surface coil, showing that the signal maintains a consistent anatomical position regardless of the surface coil position. Slight variation in the images is observed due to interaction between the surface coil's inhomogeneous receive sensitivity and reconstruction algorithm.



Extended Data Figure 8: MPI visualization of phantoms simulating brain tumor imaging, real-time embolization, and tomographic angiography at clinical-scale. (a) Proof-of-concept MPI detection of a human-derived glioblastoma tumor phantom filled with ferumoxytol. (i) A glioblastoma volume was segmented from a patient brain MRI (UPENN-GBM collection) and used to produce (ii) a 3D printed, hollow, fillable tumor phantom. (iii,iv,v) MPI scans of the phantom filled with ferumoxytol at (iii) 1.0 mg Fe (iv) 0.6 mg Fe and (v) 0.3 mg Fe, represent 0.2%, 0.12% and 0.06% of approved dose 510 mg, respectively. MPI demonstrates concentration-dependent signal at human scale. **(b)** Real-time 2D axial slice imaging at 0.8 frames/second of a trans-arterial embolization liver phantom being filled with ferucarbotran (see also **Supplemental Video SV2**). (i) Photo of the phantom prior to filling with tracer. (ii,iii) Frame grabs from real-time imaging of the phantom filling with tracer. Each image is a 2D slice, 20 × 20 cm. (iv) Final frame taken after filling that shows multiple branches did not fill with tracer. **(c)** (i,ii) Photos of phantom modeling arterial anatomy based on a 2D MRI image, filled with ferucarbotran. Approximate human-sized Styrofoam head for scale. (iii) A two-scan MPI image was taken, with rotation of the phantom by 90 degrees between scans to simulate the use of a multi-axis drive field. The two scans were aligned and summed to yield the final image.

Extended Data Table 2: Human study results & data model best-fit estimates.

(a) All human subjects, with & without magnetic tracer injection

Body Part	**Foot**						**Head**			
Subject ID	S01	S02	S03	S06	S04	S05	S01	S06	S05	S04
Age	49	45	39	29	44	29	50	29	29	44
Sex	F	M	M	F	M	M	F	F	M	M
Injected iron dose, volume	n/a	n/a	n/a	n/a	**7.5 mg, 0.5 mL**	**15 mg, 1 mL**	n/a	n/a	**7.5 mg, 0.5 mL**	**15 mg, 1 mL**
Imaging sessions	1	1	1	1	6	6	1	1	7	6
Study duration	1 day	1 day	1 day	1 day	27 weeks	28 weeks	1 day	1 day	20 weeks	12 weeks
PNS threshold, peak drive field	>3.5 mT	>3.5 mT	>3.5 mT	>3.5 mT	>3.5 mT	>3.5 mT	>3.5 mT	>3.5 mT	>3.5 mT	3.2* mT
Adverse events (CTCAE v5.0)	none	none	none	none	skin discoloration (grade 1)	skin discoloration (grade 1)	none	none	skin discoloration (grade 1)	skin discoloration (grade 1), pain at injection site (grade 1)

*50% probability from logistic curve fit

(b) Human and animal pharmacokinetic best-fit parameter estimates

		Human Foot		**Human Head**		**Murine Foot**		
		7.5 mg ferumoxytol (AMAG)	**15 mg ferumoxytol (AMAG)**	**7.5 mg ferumoxytol (AMAG)**	**15 mg ferumoxytol (Sandoz)**	n=7 ferumoxytol (AMAG)	n=3 ferumoxytol (Sandoz)	n=3 ferucarbotran (Meito)
Injection site $y = A_1 e^{-t/\tau_1} + A_2 e^{-t/\tau_2}$	A_1	4.9 mg	15.1 mg	2.8 mg	11.4 mg	78.3 %ID	81.0 %ID	27.2 %ID
	τ_1	19.7 hr	11.1 hr	29.5 hr	18.7 hr	1.9 hr	1.8 hr	23.1 hr
	A_2	1.2 mg	0.8 mg	1.9 mg	4.4 mg	24.5 %ID	20.5 %ID	72.9 %ID
	τ_2	23.7 weeks	25.3 weeks	18.6 weeks	20.1 weeks	8.3 weeks	6.9 weeks	10.3 weeks
Lymphatics $y = \frac{A(e^{-t/\tau_1} - e^{-t/\tau_2})}{(1/\tau_1)-(1/\tau_2)} + C$	A	*N/A*	*N/A*	-0.0054 a.u./hr	-0.0082 a.u./hr	-79.8 %ID/day	-50.9 %ID/day	-75.3 %ID/day
	τ_1	*N/A*	*N/A*	13.7 hr	14.1 hr	1.1 hr	2.2 hr	1.6 hr
	τ_2	*N/A*	*N/A*	5.1 days	9.4 days	53.6 days	43.1 days	52.1 days
	C	*N/A*	*N/A*	0.021 a.u.	0.037 a.u.	Model set $C = 0$	Model set $C = 0$	Model set $C = 0$

Methods

MPI Clinical Imager. An MPI image is acquired by moving a field-free region throughout a field of view, applying a drive field, and measuring signals induced in receive coils by magnetic tracers. The saturation of the tracer's magnetic response in a strong field enables spatial encoding of signals near the instantaneous position of the field free region[25,56,57] (**Extended Data Figure 1**). In this work, a field free point (FFP) is generated by a main magnet and shifted both magnetically and mechanically to cover the field of view. A drive assembly produces a pure sinusoidal field only within the field of view, and volume and surface receive coils detect the signal produced by the tracers. These subsystems are controlled using a realtime controller (National Instruments, Austin, TX) and all imaging is performed in a magnetically shielded room (ETS-Lindgren, Cedar Park, TX). Complete system specifications are provided in **Extended Data Table 1**.

The main magnet produces a strong gradient field containing a single point where the total magnetic field passes through zero, the FFP, and electronically shifts the FFP across a FOV (**Extended Data Figure 2,3)**. The main magnet is constructed using four electromagnets arranged in a quadrupolar configuration on an iron yoke. The gradient is generated by applying dc currents, and transverse (x, y) shifting is performed by superimposing additional time-varying currents. The gradient strength at the FFP is 0.3 × 0.3 × 0.6 T/m, and typical shifting fields of +/- 36 mT allow sampling across an axial (x/y) slab up to 24 cm × 24 cm. The magnet is constructed using water-cooled hollow conductors, driven using current-controlled amplifiers (IECO Oy, Helsinki, Finland), and dissipates ~80 kW during operation. The FOV is sampled axially (z) in discrete slabs by mechanically stepping the subject bed position across a 30 cm range.

The drive field interacts with the magnetic tracer to produce a signal. The field is a homogenous, axially oriented (z), sinusoidally varying magnetic field at a frequency of 45.03 kHz and an amplitude of up to 3.5 mT peak at the isocenter (**Extended Data Figure 2,5**). The drive field (referred to interchangeably as "transmit") is produced by a water-cooled resonant solenoid coil and capacitor bank (Celem Capacitors, Jerusalem, Israel) mounted to the subject bed. The coil is powered by an industrial audio-frequency amplifier (8504, AE Techron, Elkhart, IN) whose output is filtered with a balanced, fourth order passive filter. The drive field signal chain dissipates up to 875 W, with 550 W dissipated into the transmit coil, 50 W dissipated in the bore due to induced eddy currents, and 275 W into the filter. During operation, active feedback control maintains transmit phase and amplitude.

Volume and surface receive coils inductively detect signals from magnetic tracers within the FOV. A pair of volume coils (**Extended Data Figure 5**), whose winding patterns are inspired by Hadamard encoding, are mounted concentrically inside the drive coil. The first receive coil is a 2-part (+1, -1) gradiometer, and the second receive coil is a 3-part gradiometer (+1/2, -1, +1/2), each wound to minimize feedthrough from the transmitter. Each gradiometer part has a typical operating voltage of up to ~1.4 kVp, and the sum of the parts cancels the voltage at the coil output to a manageable <10 Vp. While each volume coil individually has null regions within the field of view, the coils are designed with complementary sensitivity patterns so that when combined during reconstruction, they provide uniform signal coverage across the field of view without sensitivity null regions. In contrast to the uniform sensitivity of the volume coils, the sensitivity of the surface coils varies spatially and drops off with distance from the coil's surface, which can be used to selectively detect signals from a desired region of interest. Surface coils (**Extended Data Figure 6**) are mounted to a rigid application-specific head cradle positioned inside the volume coils. The cradle accurately locates up to four surface coils next to the cervical and auricular lymph node regions. Each surface coil conductor is constructed as a printed circuit board and designed with a conductor winding optimized for high sensitivity at distances of 1.5-3 cm from the coil surface while minimizing coupling to the volume transmit coil. Human data presented utilized a left-side only coil configuration, as magnetic tracer

injections were in the left parietal scalp and subjects showed unilateral lymphatic drainage. The voltages from the 4 receive channels, 2 volume and 2 surface, are filtered with a balanced-input passive notch filter (133 dB attenuation) to remove remaining feedthrough from the transmitter prior to amplification with a custom low-noise preamplifier with a differential input based on the JFE2140 (Texas Instruments, Dallas, Texas, USA).

An imaging pulse sequence acquires a 3D volume up to 24 × 24 × 30 cm by acquiring axial slabs with mechanical bed shifts between slabs (**Extended Data Figure 2c**). For each slab, a raster acquisition sequence applies a magnetic field gradient, shifts the FFP position electronically across x and y using a triangular waveform, and applies a drive field along z. A slab acquisition covers FOVxy = 20-24 cm, typically with y-direction fast shift at 4 traversals per second and an electronic raster step size of dx = 5 mm. Axial coverage (FOVz) is typically 10-28 cm with mechanical step size of dz = 5 mm to provide sufficient spatial encoding[58]. For FOVz = 28 cm, total scan time is approximately 15 minutes. Sequence parameters for all MPI images taken on the clinical scanner are reported in **Supplementary Table ST1**.

Magnetic Tracers. Phantom, preclinical, and clinical studies utilized ferumoxytol and the active ingredient in ferucarbotran, dextran magnetite (Meito Co. Ltd., Nagoya, Japan), which we refer to as ferucarbotran in this document. Ferumoxytol is an iron oxide coated with polyglucose sorbitol carboxymethylether with a 17-31 nm hydrodynamic diameter[29], and is approved for iron replacement therapy[29] and cancer neuroimaging[30]. Ferumoxytol was obtained from two manufacturers, AMAG Pharmaceuticals (Feraheme; Waltham, MA, USA) and Sandoz (generic; Basel, Switzerland). Ferucarbotran is an iron oxide coated with carboxydextran with a ~57 nm hydrodynamic diameter[47], and is approved for human use as an MRI contrast agent in Germany and Sweden (Resotran; B.E. Imaging GmbH, Baden-Baden, Germany)[59] and Japan (Resovist; PDR Pharma Co. Ltd., Tokyo, Japan)[60], and was not available for our study. Magtrace, an FDA-approved medical device for SLNB procedures[35] with MPI imaging performance comparable to ferucarbotran (data not shown), was also not available for our study.

Signal Processing & Image Reconstruction. The analog signals are digitized at 4 MSPS by the realtime controller and digitally filtered to isolate the 90-250 kHz frequency band. The time domain signals are transformed into harmonic portraits $d_k(x,y,z)$ (where k=harmonic number), by filtering harmonic bands of the drive field frequency and gridding them to the instantaneous FFP position (**Extended Data Figure 1b**). The harmonic portraits are reconstructed into volume or surface coil specific images using multi-harmonic gridded 3D deconvolution (MH3D)[58], which is a convolutional forward model that incorporates the transmit and receive coil sensitivity patterns and the magnetic tracer's point spread function.

For each scan, volume coil images and, when applicable, surface coil images are reconstructed. When both are used, the images are typically combined using coil sensitivity-weighting into a single composite image displayed in a perceptually linear false color colormap designed for MPI ("bluesteel", black-blue-gold, **Supplemental Figure S2, Supplemental Table ST2**). However, in the case of ferumoxytol at high dynamic range, low native resolution and low sensitivity worsen shine-through artifact and reconstruction noise, making a single composite visualization challenging. Therefore, to better visualize the surface coil signal with this tracer, we display the volume coil data in grayscale and the surface coil data in bluesteel as separate overlays rather than compositing them into a single image. In all cases, resulting MPI images are displayed either as maximum intensity projections (MIPs) created using MATLAB (2024b, MathWorks, Natick MA) or as volume renderings co-registered with an optical scan or X-ray CT using 3D Slicer[61].

Basic Safety. The imager was verified using a risk-based approach against a subset of requirements defined by the IEC and FDA for MRI, in this work defined as "basic safety" testing. Our verifications in-

cluded general requirements for medical equipment[62], with a focus on electrical safety. For MPI-specific verifications arising from the use of time-varying magnetic fields[63], we evaluated the imager against MRI guidance for Specific Absorption Rate (SAR) in order to support Nonsignificant Risk determination and performed magnetostimulation studies to determine stimulation thresholds in human heads and feet[64–66]. We detail the SAR and magnetostimulation testing below.

Specific Absorption Rate (SAR) Simulation and Phantom Testing. SAR was simulated on an anatomically realistic virtual human body model ("Duke") and a saline phantom using Sim4Life (ZMT Zurich MedTech AG) and experimentally verified for the phantom (**Figure 3**). See **Supplementary Methods** for details.

Human PNS Threshold Simulation. Peripheral nerve stimulation (PNS) is the activation of nerves in response to a time-varying magnetic field. Electromagnetic simulations were performed to determine the onset of PNS in a virtual body model for the drive field conductor up to 7 mT peak. The simulation used the Sim4Life software and estimated the onset of PNS using the drive field conductor model used in the SAR simulations, the "Yoon-sun" virtual human body models, and the NEURON Solver implementing the "McIntyre-Richardson-Grill" (MRG) neuronal model.

Human Magnetostimulation Threshold Testing. The magnetostimulation threshold studies were designed to measure the onset of PNS and/or magnetophosphenes, primarily informing the selection of imaging sequence parameters. When experienced by a subject, the PNS stimulation at threshold is experienced as a perceptible activation of peripheral nerves such as light tingling or twitching, and magnetophenes at threshold are experienced as faint flickering visual sensations[64]. Prior experimental MPI human PNS testing focused on the drive fields[67–69]. Here we test all magnetic fields used in an imaging sequence. The study was approved by the Advarra (Protocol #Pro00071449) Institutional Review Board and the Stanford Institutional Review Board via reliance.

Magnetostimulation thresholds were measured in 6 healthy adult subjects (n=6 feet, n=4 head). The study used a systematic protocol to isolate effects of each magnetic field component for the gradient, shift, drive field, as well as combinations of all the fields. For each configuration, field amplitude was first increased in coarse steps up to the maximum amplitude. During testing, subjects reported any sensations or visual perceptions. In the event of stimulation, the process is then repeated with finer step sizes starting below the coarse threshold. Last, the subject is tested with random amplitudes within ±15% of the fine threshold. Because higher frequencies (e.g., >10 kHz) tend not to have a sharp transition at the stimulation threshold, this fine sampling and statistical modeling approach enables accurate and consistent measurement of the amplitude at which a subject has a 50% probability of stimulation[67]. To determine this 50% probability amplitude, the binary magnetostimulation data was fit to a logistic regression (**Figure 3f**).

Study demographics and results are shown in **Extended Data Table 2** and **Figure 3**. For subjects that experienced magnetostimulation, results were used to set field amplitudes for subsequent imaging experiments.

Human Imaging with Tracer Injection. A subset of subjects enrolled in optional human imaging with tracer injection substudies. The substudy enrolled 2 healthy adult subjects (n=2 feet, n=2 head). The study was approved by the Advarra (Protocol #Pro00071449) Institutional Review Board and the Stanford Institutional Review Board via reliance. Adverse events were classified using the Common Terminology

Criteria for Adverse Events (CTCAE) v5.0[70]; if the adverse event was not specifically listed in the CTCAE, the general grading guidelines were applied.

For the head injections (n=2), subcutaneous injections were performed in the parietal scalp. For the foot injections (n=2), subcutaneous injections were performed in the lateral heel, between the lateral malleolus and Achilles tendon. The tracer injected in all cases was ferumoxytol, manufactured by either AMAG Pharmaceuticals or Sandoz (see table below). All dilutions were performed immediately prior to injection in a 1:1 ratio with sterile saline. All injections were performed by a physician at Stanford University Medical School, Stanford, California, USA.

Injection details by anatomy and subject:

Anatomy	Subject	Ferumoxytol Source	Iron Quantity	Injection Volume
Head	S05	AMAG Pharma.	7.5 mg	0.5 mL
Head	S04	Sandoz	15.0 mg	1.0 mL
Foot	S04	AMAG Pharma.	7.5 mg	0.5 mL
Foot	S05	AMAG Pharma.	15.0 mg	1.0 mL

Following injection, the subject was monitored for 30 minutes, then transported to the study site and first underwent repeat magnetostimulation protocol, resulting in a ~2 hr delay before the first imaging timepoint.

Longitudinal imaging was performed via multiple imaging sessions post-injection. To capture expected tracer clearance rates, imaging sessions occurred more frequently in the week following injection (day 1–3, etc.) and then more widely spaced through the experimental window (1 week–6 months). While consistent sequence parameters were targeted for longitudinal imaging of injection sites, the exploratory nature of the lymphatic imaging resulted in some variation in sequence parameters. Sequence parameters for all images used in the analysis are specified in **Supplementary Table ST1**.

The injection site was photographed after each imaging session to monitor skin discoloration. Subjects were scanned with a 3D camera (Einstar Vega, Shining 3D, Hangzhou, China). MPI and optical scans were co-registered using MPI/optically-visible fiducials in 3D Slicer[61].

Human Data Image Analysis & Quantitative Calibration. Injection sites and lymphatic regions were analyzed using region-specific image processing workflows. For the injection site, signal was quantified over time and calibrated to quantify magnetic tracer quantity over time. For the lymphatic region, signal was quantified over time but not calibrated, due to higher signal variability caused by scan-to-scan changes in subject positioning and in imaging sequence parameters, complicated by the field nonuniformity in the surface coils.

Injection site signal quantification was performed by integrating the signal over a 3D rectangular prism ROI_{Inj} (10 × 10 × 4 cm) of the volume coil reconstruction (V) for each image in the time series (**Figure 2a**).

Injection site signal calibration established an integrated signal-to-tracer quantity scaling factor using a phantom modeling the injection site. The phantom was constructed by loading a 2.25 cm disc-shaped cotton absorbent pad with tracer matching the subject's injection quantity and volume. The pad was used to mimic the distribution of tracer following subcutaneous injections. It was placed in a resealable plastic sleeve, and affixed to a head phantom at the approximate injection site location for imaging using the same sequence and parameters.

Head-and-neck lymph node region signal quantification was performed by integrating the signal over a 3D

rectangular prism ROI_{LNs} of the surface coil reconstruction (S) for each image in the time series **(Figure 2a)**. Only the surface coil reconstruction was used, as the volume coils lacked sufficient sensitivity and shine-through performance for imaging ferumoxytol in the lymph nodes. With ferumoxytol's low spatial resolution, individual lymph nodes were not expected to be resolvable, so signal was integrated over the entire region rather than reported for individual nodes. The ROI_{LNs} dimensions (S04: 14 × 14 × 12 cm, S05: 12 × 14 × 10 cm) were set for each subject, and consistent across all longitudinal time points (**Supplemental Table ST1)**.

Time-Series Data Analysis. Time-series analysis was performed by fitting parametric models in MATLAB (2024b, MathWorks, Natick MA). The injection site was modeled assuming monotonic tracer clearance. Lymphatic uptake and clearance were modeled assuming signal accumulation and decay occur concurrently. Best-fit parameter estimates are reported in **Extended Data Table 2b**. The time-series analyses were performed independently for the injection site and lymph node regions. Sequence parameters for all images used in each analysis are listed by figure in **Supplemental Data Table ST1**.

Injection site clearance dynamics were modeled by a bi-exponential decay, and the decay time values are reported for a least-squares fit to measured data using a solver built on nonlinear Nelder-Mead optimization (*fminsearch*). Prediction intervals (95%) were estimated using a parametric bootstrap with Student-t noise and a small-sample variance correction to avoid undercoverage given limited data points[71]. The images used in the injection site time-series analysis were acquired using a predefined imaging sequence and subject position.

Lymphatic update and clearance dynamics were modeled by a two-pole overdamped model, which can be shown equivalent to a two-compartment model[72], and the time constants are reported for a least-squares fit to measured data. Parameters and their 95% prediction intervals were estimated by nonlinear least-squares regression (*fitnlm*). The images used in the lymphatic time-series analysis pooled a few groupings (detailed in **Supplementary Table ST1**) of imaging sequence parameters and head rotation positions (positions illustrated in **Extended Data Figure 7a**). The pooling balanced time-course sampling density with the high image-to-image parameter variability. Error bars in **Figure 2d** show the average and standard deviation for images grouped by same acquisition day.

Imaging Performance Characterization. The system performance was characterized for spatial resolution, shine-through, and sensitivity using phantoms with both ferumoxytol and ferucarbotran (see **Extended Data Figures 4-6** and **Supplementary Methods** for details).

Imaging Performance Benchmarking with SPECT and Gamma Camera. Phantom studies were completed to benchmark MPI image quality against Tc-99m scintigraphy and SPECT in head and neck lymphatic imaging. A phantom was constructed from a Styrofoam mannequin head (SmoothFōM® Male Foam Head, FloraCraft®, Ludington, Michigan) with holes for a 1.5 mL tube in the left parietal scalp to model the injection site, and eleven 0.2 mL tubes in periauricular and cervical regions to model draining lymph nodes on the same (left). Images were acquired on the phantoms using planar scintigraphy, SPECT, MPI with ferucarbotran and MPI with ferumoxytol. See **Supplementary Methods** for details.

Preclinical Animal Testing & Tracer Relaxometry. Mouse tracer pharmacokinetics studies were conducted at the Robarts Research Institute under an approved protocol from Western University's Institutional Animal Care and Use Committee (Protocol #2023-113) and adhered to ARRIVE guidelines.

Mice received subcutaneous hind-footpad injections of one of three tracers: ferumoxytol manufactured by AMAG Pharmaceuticals (50 µg, n=7), ferumoxytol manufactured by Sandoz (50 µg, n=3), or ferucarbotran (25 µg, n=6) in a volume of 25 µL.

MPI images were acquired on a preclinical MPI scanner (Momentum, Magnetic Insight Inc., Alameda, CA) at multiple time points up to 8 weeks post-injection to quantify magnetic tracer pharmacokinetics.

At study endpoint, mice were euthanized and the popliteal and iliac lymph nodes were excised and processed for Perl's Prussian blue staining to confirm iron deposition.

Magnetic properties of ferumoxytol (AMAG Pharmaceuticals vs. Sandoz) were characterized using magnetic particle relaxometry (RELAX module, Momentum™, Magnetic Insight Inc, Alameda, CA).

Methods References

56. Goodwill, P. W. & Conolly, S. M. The X-Space Formulation of the Magnetic Particle Imaging Process: 1-D Signal, Resolution, Bandwidth, SNR, SAR, and Magnetostimulation. *IEEE Transactions on Medical Imaging* **29,** 1851–1859. ISSN: 0278-0062. http://ieeexplore.ieee.org/document/5482192/ (Nov. 2010).
57. Goodwill, P. W., Konkle, J. J., Zheng, B., Saritas, E. U. & Conolly, S. M. Projection X-Space Magnetic Particle Imaging. *IEEE Transactions on Medical Imaging* **31,** 1076–1085. ISSN: 0278-0062. http://ieeexplore.ieee.org/document/6144743/ (May 2012).
58. Sanders, T., Konkle, J. J., Mason, E. E. & Goodwill, P. W. Multi-Harmonic Gridded 3D Deconvolution (MH3D) for Robust and Accurate Image Reconstruction in MPI for Single Axis Drive Field Scanners. *Physics in Medicine & Biology* (2025).
59. B.E. Imaging GmbH. *Resotran (ferucarbotran injection) product information* Apr. 2024. https://www.fachinfo.de/pdf/023940.
60. PDR Pharma Co. Ltd. *Resovist (ferucarbotran injection) Prescribing Information* Mar. 2022. https://pins.japic.or.jp/pdf/newPINS/00049238.pdf.
61. Federov, A. *et al. 3D Slicer as an Image Computing Platform for the Quantitative Imaging Network* 2012.
62. International Electrotechnical Commission. *IEC 60601-1(3.2b) Medical electrical equipment: General requirements for basic safety and essential performance* tech. rep. (Aug. 2020). www.iec.ch.
63. Schmale, I. *et al.* MPI Safety in the View of MRI Safety Standards. *IEEE Transactions on Magnetics* **51,** 6502604. ISSN: 00189464 (2015).
64. International Electrotechnical Commission. *IEC 60601-2-33:2022 Medical electrical equipment: Particular requirements for the basic safety and essential performance of magnetic resonance equipment for medical diagnosis* tech. rep. (Aug. 2022).
65. Food and Drug Administration. *Criteria for Significant Risk Investigations of Magnetic Resonance Diagnostic Devices, Guidance for Industry and Food and Drug Administration Staff* tech. rep. (June 2014). www.fda.gov/media/71385/download.
66. National Electrical Manufacturers Association (NEMA). *NEMA Standards Publication MS 8-2016: Characterization of the Specific Absorption Rate (SAR) for Magnetic Resonance Imaging Systems* 2023. https://www.nema.org/standards/view/Characterization-of-the-Specific-Absorption-Rate-for-Magnetic-Resonance-Imaging-Systems.
67. Saritas, E. U., Goodwill, P. W., Zhang, G. Z. & Conolly, S. M. Magnetostimulation limits in magnetic particle imaging. *IEEE Transactions on Medical Imaging* **32,** 1600–1610. ISSN: 02780062 (2013).

68. Barksdale, A. C. *et al.* Measurement of peripheral nerve magnetostimulation thresholds of a head solenoid coil between 200 Hz and 88.1 kHz. *Research Square,* rs.3.rs–4864083. https://pmc.ncbi.nlm.nih.gov/articles/PMC11527250/ (Oct. 2024).
69. Schmale, I. *et al.* Human PNS and SAR study in the frequency range from 24 to 162 kHz. *2013 International Workshop on Magnetic Particle Imaging* (2013).
70. U.S. Department of Health and Human Services. *Common Terminology Criteria for Adverse Events (CTCAE) v5.0* tech. rep. (2017). https://dctd.cancer.gov/research/ctep-trials/for-sites/adverse-events/ctcae-v5-8x11.pdf.
71. Pan, L. & Politis, D. N. *Bootstrap prediction intervals for linear, nonlinear and nonparametric autoregressions* tech. rep. ().
72. Fan, X. & Karczmar, G. S. A new approach to analysis of the impulse response function (IRF) in dynamic contrast-enhanced MRI (DCEMRI): A simulation study. *Magnetic Resonance in Medicine* **62,** 229–239. ISSN: 15222594 (2009).
73. Nieuwenhuis, E. R. *et al.* Performance of a Nonlinear Magnetic Handheld Probe for Intraoperative Sentinel Lymph Node Detection: A Phantom Study. *Annals of Surgical Oncology* **30,** 8735–8742. ISSN: 15344681 (Dec. 2023).
74. Mirzaei, N. *et al.* Sentinel lymph node localization and staging with a low-dose of superparamagnetic iron oxide (SPIO) enhanced MRI and magnetometer in patients with cutaneous melanoma of the extremity - The MAGMEN feasibility study. *European Journal of Surgical Oncology* **48,** 326–332. ISSN: 0748-7983 (Feb. 2022).

Supplementary Methods

Black text is repeated from Methods. Blue text provides additional details only present in Supplementary Methods.

MPI Clinical Imager. An MPI image is acquired by moving a field-free region throughout a field of view, applying a drive field, and measuring signals induced in receive coils by magnetic tracers. The saturation of the tracer's magnetic response in a strong field enables spatial encoding of signals near the instantaneous position of the field free region[25,56,57] (**Extended Data Figure 1**). In this work, a field free point (FFP) is generated by a main magnet and shifted both magnetically and mechanically to cover the field of view. A drive assembly produces a pure sinusoidal field only within the field of view, and volume and surface receive coils detect the signal produced by the tracers. These subsystems are controlled using a realtime controller (National Instruments, Austin, TX) and all imaging is performed in a magnetically shielded room (ETS-Lindgren, Cedar Park, TX). Complete system specifications are provided in **Extended Data Table 1**.

The main magnet produces a strong gradient field containing a single point where the total magnetic field passes through zero, the FFP, and electronically shifts the FFP across a FOV (**Extended Data Figure 2,3)**. The main magnet is constructed using four electromagnets arranged in a quadrupolar configuration on an iron yoke. The gradient is generated by applying dc currents, and transverse (x, y) shifting is performed by superimposing additional time-varying currents. The gradient strength at the FFP is 0.3 × 0.3 × 0.6 T/m, and typical shifting fields of +/- 36 mT allow sampling across an axial (x/y) slab up to 24 cm × 24 cm. The magnet is constructed using water-cooled hollow conductors, driven using current-controlled amplifiers (IECO Oy, Helsinki, Finland), and dissipates ~80 kW during operation. The FOV is sampled axially (z) in discrete slabs by mechanically stepping the subject bed position across a 30 cm range.

The drive field interacts with the magnetic tracer to produce a signal. The field is a homogenous, axially oriented (z), sinusoidally varying magnetic field at a frequency of 45.03 kHz and an amplitude of up to 3.5 mT peak at the isocenter (**Extended Data Figure 2,5**). The drive field (referred to interchangeably as "transmit") is produced by a water-cooled resonant solenoid coil and capacitor bank (Celem Capacitors, Jerusalem, Israel) mounted to the subject bed. The coil is powered by an industrial audio-frequency amplifier (8504, AE Techron, Elkhart, IN) whose output is filtered with a balanced, fourth order passive filter. The drive field signal chain dissipates up to 875 W, with 550 W dissipated into the transmit coil, 50 W dissipated in the bore due to induced eddy currents, and 275 W into the filter. During operation, active feedback control maintains transmit phase and amplitude.

Volume and surface receive coils inductively detect signals from magnetic tracers within the FOV. A pair of volume coils (**Extended Data Figure 5**), whose winding patterns are inspired by Hadamard encoding, are mounted concentrically inside the drive coil. The first receive coil is a 2-part (+1, -1) gradiometer, and the second receive coil is a 3-part gradiometer (+1/2, -1, +1/2), each wound to minimize feedthrough from the transmitter. Each gradiometer part has a typical operating voltage of up to ~1.4 kVp, and the sum of the parts cancels the voltage at the coil output to a manageable <10 Vp. While each volume coil individually has null regions within the field of view, the coils are designed with complementary sensitivity patterns so that when combined during reconstruction, they provide uniform signal coverage across the field of view without sensitivity null regions. In contrast to the uniform sensitivity of the volume coils, the sensitivity of the surface coils varies spatially and drops off with distance from the coil's surface, which can be used to selectively detect signals from a desired region of interest. Surface coils (**Extended Data Figure 6**) are mounted to a rigid application-specific head cradle positioned inside the volume coils. The cradle accurately locates up to four surface coils next to the cervical and auricular lymph node regions. Each surface

coil conductor is constructed as a printed circuit board and designed with a conductor winding optimized for high sensitivity at distances of 1.5-3 cm from the coil surface while minimizing coupling to the volume transmit coil. Human data presented utilized a left-side only coil configuration, as magnetic tracer injections were in the left parietal scalp and subjects showed unilateral lymphatic drainage. The voltages from the 4 receive channels, 2 volume and 2 surface, are filtered with a balanced-input passive notch filter (133 dB attenuation) to remove remaining feedthrough from the transmitter prior to amplification with a custom low-noise preamplifier with a differential input based on the JFE2140 (Texas Instruments, Dallas, Texas, USA).

An imaging pulse sequence acquires a 3D volume up to 24 × 24 × 30 cm by acquiring axial slabs with mechanical bed shifts between slabs (**Extended Data Figure 2c**). For each slab, a raster acquisition sequence applies a magnetic field gradient, shifts the FFP position electronically across x and y using a triangular waveform, and applies a drive field along z. A slab acquisition covers FOVxy = 20-24 cm, typically with y-direction fast shift at 4 traversals per second and an electronic raster step size of dx = 5 mm. Axial coverage (FOVz) is typically 10-28 cm with mechanical step size of dz = 5 mm to provide sufficient spatial encoding[58]. For FOVz = 28 cm, total scan time is approximately 15 minutes. Sequence parameters for all MPI images taken on the clinical scanner are reported in **Supplementary Table ST1**.

Magnetic Tracers. Phantom, preclinical, and clinical studies utilized ferumoxytol and the active ingredient in ferucarbotran, dextran magnetite (Meito Co. Ltd., Nagoya, Japan), which we refer to as ferucarbotran in this document. Ferumoxytol is an iron oxide coated with polyglucose sorbitol carboxymethylether with a 17-31 nm hydrodynamic diameter[29], and is approved for iron replacement therapy[29] and cancer neuroimaging[30]. Ferumoxytol was obtained from two manufacturers, AMAG Pharmaceuticals (Feraheme; Waltham, MA, USA) and Sandoz (generic; Basel, Switzerland). Ferucarbotran is an iron oxide coated with carboxydextran with a ~57 nm hydrodynamic diameter[47], and is approved for human use as an MRI contrast agent in Germany and Sweden (Resotran; B.E. Imaging GmbH, Baden-Baden, Germany)[59] and Japan (Resovist; PDR Pharma Co. Ltd., Tokyo, Japan)[60], and was not available for our study. Magtrace, an FDA-approved medical device for SLNB procedures[35] with MPI imaging performance comparable to ferucarbotran (data not shown), was also not available for our study.

Signal Processing & Image Reconstruction. The analog signals are digitized at 4 MSPS by the realtime controller and digitally filtered to isolate the 90-250 kHz frequency band. The time domain signals are transformed into harmonic portraits $d_k(x,y,z)$ (where k=harmonic number), by filtering harmonic bands of the drive field frequency and gridding them to the instantaneous FFP position (**Extended Data Figure 1b**). The harmonic portraits are reconstructed into volume or surface coil specific images using multi-harmonic gridded 3D deconvolution (MH3D)[58], which is a convolutional forward model that incorporates the transmit and receive coil sensitivity patterns and the magnetic tracer's point spread function.

The MH3D convolutional forward model[58] shapes the reconstruction point spread function and background noise such that integrated signal remains constant regardless of ROI size provided the signal is fully encompassed. This property enables quantitation using simple geometric ROIs rather than anatomically shaped regions.

For each scan, volume coil images and, when applicable, surface coil images are reconstructed. When both are used, the images are typically combined using coil sensitivity-weighting into a single composite image displayed in a perceptually linear false color colormap designed for MPI ("bluesteel", black-blue-gold, **Supplemental Figure S2, Supplemental Table ST2**). However, in the case of ferumoxytol at high dynamic range, low native resolution and low sensitivity worsen shine-through artifact and reconstruction

noise, making a single composite visualization challenging. Therefore, to better visualize the surface coil signal with this tracer, we display the volume coil data in grayscale and the surface coil data in bluesteel as separate overlays rather than compositing them into a single image. In all cases, resulting MPI images are displayed either as maximum intensity projections (MIPs) created using MATLAB (2024b, MathWorks, Natick MA) or as volume renderings co-registered with an optical scan or X-ray CT using 3D Slicer[61].

Basic Safety. The imager was verified using a risk-based approach against a subset of requirements defined by the IEC and FDA for MRI, in this work defined as "basic safety" testing. Our verifications included general requirements for medical equipment[62], with a focus on electrical safety. For MPI-specific verifications arising from the use of time-varying magnetic fields[63], we evaluated the imager against MRI guidance for Specific Absorption Rate (SAR) in order to support Nonsignificant Risk determination and performed magnetostimulation studies to determine stimulation thresholds in human heads and feet[64–66]. We detail the SAR and magnetostimulation testing below.

Specific Absorption Rate (SAR) Simulation and Phantom Testing. SAR was simulated on an anatomically realistic virtual human body model ("Duke") and a saline phantom using Sim4Life (ZMT Zurich MedTech AG) and experimentally verified for the phantom (**Figure 3**). See **Supplementary Methods** for details.

The simulations modeled only the drive field conductor, and simulated a 7 mT peak drive field, which was twice the field strength used in the study. Simulations were performed by Tesla Dynamic Coils (Zaltbommel, Netherlands).

SAR testing was performed by adapting standardized methods used in MRI (NEMA MS 8-2016[66]). The phantom was constructed using an LDPE carboy and insulated with Styrofoam. Due to the expected low SAR, the conductivity of the phantom was higher than physiological conductivity to allow for sufficient heating for reliable measurements. Measurements were performed on the insulated phantom at a 3.5 mT peak drive field utilizing a high accuracy thermometer and probe (TTI-10 Precision Thermometer, IsoTech, Colchester, Vermont), and the results compared with simulation.

Human PNS Threshold Simulation. Peripheral nerve stimulation (PNS) is the activation of nerves in response to a time-varying magnetic field. Electromagnetic simulations were performed to determine the onset of PNS in a virtual body model for the drive field conductor up to 7 mT peak. The simulation used the Sim4Life software and estimated the onset of PNS using the drive field conductor model used in the SAR simulations, the "Yoon-sun" virtual human body models, and the NEURON Solver implementing the "McIntyre-Richardson-Grill" (MRG) neuronal model.

Human Magnetostimulation Threshold Testing. The magnetostimulation threshold studies were designed to measure the onset of PNS and/or magnetophosphenes, primarily informing the selection of imaging sequence parameters. When experienced by a subject, the PNS stimulation at threshold is experienced as a perceptible activation of peripheral nerves such as light tingling or twitching, and magnetophenes at threshold are experienced as faint flickering visual sensations[64]. Prior experimental MPI human PNS testing focused on the drive fields[67–69]. Here we test all magnetic fields used in an imaging sequence. The study was approved by the Advarra (Protocol #Pro00071449) Institutional Review Board and the Stanford Institutional Review Board via reliance.

Exclusion criteria for the study was:

1. Active implants in any part of the body, including but not limited to: Pacemakers, drug ports with metal, implanted stimulator devices, including cochlear implants, deep brain stimulators, vagus nerve stimulators, other implanted electrodes or stimulators.
2. Indwelling medical devices that contain metal in the head, including but not limited to: Aneurysm clips or coils and stents.
3. Copper IUD.
4. Known or suspected pregnancy – a pregnancy test will be required for women of child-bearing potential.
5. History of work in the metal working industry.
6. History of known or suspected orbital metal foreign bodies.
7. History of claustrophobia.
8. History of migraines, epilepsy, or seizure.
9. History of heart rhythm disturbances.
10. Weight greater than 250 lbs.
11. Unable to comfortably fit inside the imager region where the magnetic fields are generated and detected.

Additional exclusion criteria for foot testing:

1. Unconfirmed MRI-compatible indwelling medical devices containing metal and non-removable metal objects on the foot or leg that will be scanned, including but not limited to:
   (a) Pins, plates, screws, etc.
   (b) Non-removable piercings and metal fragments.
2. Tattoos on the foot or leg that will be scanned.

Additional exclusion criteria for the head testing:

1. Unconfirmed MRI-compatible oral devices; stainless steel crowns, orthodontic devices such as permanent retainers, braces and wires, and dental implants.
2. Unconfirmed MRI-compatible indwelling medical devices containing metal and non-removable metal objects, in the head and neck, including but not limited to:
   (a) Pins, plates, screws, etc.
   (b) Non-removable piercings, metal fragments, and certain kinds of hair extensions.
3. Tattoos on the neck and head, including permanent makeup.

MRI compatibility was determined by a subject history of MRI imaging since the object was placed or by referencing the MRI compatibility database on MRIsafety.com (e.g., for example amalgam fillings are considered “safe” and were allowed for head visits).

Magnetostimulation thresholds were measured in 6 healthy adult subjects (n=6 feet, n=4 head). The study used a systematic protocol to isolate effects of each magnetic field component for the gradient, shift, drive field, as well as combinations of all the fields. For each configuration, field amplitude was first increased in coarse steps up to the maximum amplitude. During testing, subjects reported any sensations or visual perceptions. In the event of stimulation, the process is then repeated with finer step sizes starting below the coarse threshold. Last, the subject is tested with random amplitudes within ±15% of the fine threshold. Because higher frequencies (e.g., >10 kHz) tend not to have a sharp transition at the stimulation threshold, this fine sampling and statistical modeling approach enables accurate and consistent measurement of the amplitude at which a subject has a 50% probability of stimulation[67]. To determine this 50% probability amplitude, the binary magnetostimulation data was fit to a logistic regression (**Figure 3f**).

Subjects notified study personnel of magnetostimulation via a Bluetooth-enabled button, verbally confirmed stimulation had occurred, and described the location and description of sensation to the study per-

sonnel. During each session, subjects were monitored by the study doctor and a study coordinator who maintained two-way audio communication with the system operator. During scans, subjects were provided with a non-magnetic, MPI-compatible, emergency alert squeeze bulb (MagnaAlarm Panic Alarm, Magnacoustics).

Study demographics and results are shown in **Extended Data Table 2** and **Figure 3**. For subjects that experienced magnetostimulation, results were used to set field amplitudes for subsequent imaging experiments.

Human Imaging with Tracer Injection. A subset of subjects enrolled in optional human imaging with tracer injection substudies. The substudy enrolled 2 healthy adult subjects (n=2 feet, n=2 head). The study was approved by the Advarra (Protocol #Pro00071449) Institutional Review Board and the Stanford Institutional Review Board via reliance. Adverse events were classified using the Common Terminology Criteria for Adverse Events (CTCAE) v5.0[70]; if the adverse event was not specifically listed in the CTCAE, the general grading guidelines were applied.

Additional exclusion criteria for the tracer injection study beyond those seen in the magnetostimulation study included:

1. History of iron overload disease.
2. Known intolerance/hypersensitivity to iron, and/or dextran compounds, and/or Magtrace.
3. Known hypersensitivity to ferumoxytol or any of its components.
4. History of diagnosed impaired lymphatic function.
5. History of iron replacement products infusion (e.g., ferumoxytol) injection within the past 12 months.
6. Participation in an investigational drug study within 30 days from date of consent.
7. Currently breastfeeding/lactating women.

For the head injections (n=2), subcutaneous injections were performed in the parietal scalp. For the foot injections (n=2), subcutaneous injections were performed in the lateral heel, between the lateral malleolus and Achilles tendon. The tracer injected in all cases was ferumoxytol, manufactured by either AMAG Pharmaceuticals or Sandoz (see table below). All dilutions were performed immediately prior to injection in a 1:1 ratio with sterile saline. All injections were performed by a physician at Stanford University Medical School, Stanford, California, USA.

Injection details by anatomy and subject:

Anatomy	Subject	Ferumoxytol Source	Iron Quantity	Injection Volume
Head	S05	AMAG Pharma.	7.5 mg	0.5 mL
Head	S04	Sandoz	15.0 mg	1.0 mL
Foot	S04	AMAG Pharma.	7.5 mg	0.5 mL
Foot	S05	AMAG Pharma.	15.0 mg	1.0 mL

Following injection, the subject was monitored for 30 minutes, then transported to the study site and first underwent repeat magnetostimulation protocol, resulting in a ~2 hr delay before the first imaging timepoint.

For subjects that experienced magnetostimulation, imaging was typically performed at one to two standard deviations below the 50% probability amplitude, and no imaging was performed beyond 50%. Specifically, for the subject (S04) that experienced magnetostimulation in the head, most images were acquired at a 2.8 or 2.4 mT peak (50%-1σ or -2σ) drive field amplitidue, and no imaging was performed beyond $<$3.2 mT peak (50%). All other subjects (head and feet) did not experience magnetostimulation and used the maximum drive amplitude of 3.5 mT peak.

Longitudinal imaging was performed via multiple imaging sessions post-injection. To capture expected tracer clearance rates, imaging sessions occurred more frequently in the week following injection (day 1–3, etc.) and then more widely spaced through the experimental window (1 week–6 months). While consistent sequence parameters were targeted for longitudinal imaging of injection sites, the exploratory nature of the lymphatic imaging resulted in some variation in sequence parameters. Sequence parameters for all images used in the analysis are specified in **Supplementary Table ST1**.

The injection site was photographed after each imaging session to monitor skin discoloration. Subjects were scanned with a 3D camera (Einstar Vega, Shining 3D, Hangzhou, China). MPI and optical scans were co-registered using MPI/optically-visible fiducials in 3D Slicer[61].

Human Data Image Analysis & Quantitative Calibration. Injection sites and lymphatic regions were analyzed using region-specific image processing workflows. For the injection site, signal was quantified over time and calibrated to quantify magnetic tracer quantity over time. For the lymphatic region, signal was quantified over time but not calibrated, due to higher signal variability caused by scan-to-scan changes in subject positioning and in imaging sequence parameters, complicated by the field nonuniformity in the surface coils.

Injection site signal quantification was performed by integrating the signal over a 3D rectangular prism ROI_{Inj} (10 × 10 × 4 cm) of the volume coil reconstruction (V) for each image in the time series (**Figure 2a**).

Injection site signal calibration established an integrated signal-to-tracer quantity scaling factor using a phantom modeling the injection site. The phantom was constructed by loading a 2.25 cm disc-shaped cotton absorbent pad with tracer matching the subject's injection quantity and volume. The pad was used to mimic the distribution of tracer following subcutaneous injections. It was placed in a resealable plastic sleeve, and affixed to a head phantom at the approximate injection site location for imaging using the same sequence and parameters.

Additional approaches for injection site signal calibration were tested before selecting the pad-phantom scaling factor. These approaches included placing a known quantity of tracer within the field of view, and measuring a signal-to-tracer scaling curve using a dilution series. For a known quantity calibration, reference fiducials were attached to the subject during imaging (e.g., "Fid" in **Figure 1f**); however, the large signal from the higher-dose injection sites sometimes washed out signal from the fiducial, reducing calibration accuracy. For measuring a signal-to-tracer scaling curve, a serial dilution of reference vials was imaged that spanned the expected iron quantities in the image (0.625–20 mg Fe). While the dilution series confirmed linear system response, we found that the current reconstruction algorithms produce systematic quantitation errors when applied to different geometries such as point sources and broad discs.

Head-and-neck lymph node region signal quantification was performed by integrating the signal over a 3D rectangular prism ROI_{LNs} of the surface coil reconstruction (S) for each image in the time series **(Figure 2a)**. Only the surface coil reconstruction was used, as the volume coils lacked sufficient sensitivity and shine-through performance for imaging ferumoxytol in the lymph nodes. With ferumoxytol's low spatial resolution, individual lymph nodes were not expected to be resolvable, so signal was integrated over the entire region rather than reported for individual nodes. The ROI_{LNs} dimensions (S04: 14 × 14 × 12 cm, S05: 12 × 14 × 10 cm) were set for each subject, and consistent across all longitudinal time points (**Supplemental Table ST1)**.

The team experimented with adjusting sequence parameters and subject positions to identify and confirm lymphatic signal. To achieve a grouping of datasets with consistent imaging parameters for longitudinal

analysis, images were selected with defined ranges of FOVz, z step size, application-specific surface coil position, and head rotations. The remaining imaging parameter variation within these ranges likely contributes to the variance observed in the lymphatic signal time points.

Time-Series Data Analysis. Time-series analysis was performed by fitting parametric models in MATLAB (2024b, MathWorks, Natick MA). The injection site was modeled assuming monotonic tracer clearance. Lymphatic uptake and clearance were modeled assuming signal accumulation and decay occur concurrently. Best-fit parameter estimates are reported in **Extended Data Table 2b**. The time-series analyses were performed independently for the injection site and lymph node regions. Sequence parameters for all images used in each analysis are listed by figure in **Supplemental Data Table ST1**.

Injection site clearance dynamics were modeled by a bi-exponential decay, and the decay time values are reported for a least-squares fit to measured data using a solver built on nonlinear Nelder-Mead optimization (*fminsearch*). Prediction intervals (95%) were estimated using a parametric bootstrap with Student-t noise and a small-sample variance correction to avoid undercoverage given limited data points[71]. The images used in the injection site time-series analysis were acquired using a predefined imaging sequence and subject position.

Bi-exponential decays were modeled as:

$$y = A_1 e^{-t/\tau_1} + A_2 e^{-t/\tau_2} \tag{1}$$

where A_1 and A_2 are amplitudes and τ_1 and τ_2 are the fast and slow time constants.

Lymphatic update and clearance dynamics were modeled by a two-pole overdamped model, which can be shown equivalent to a two-compartment model[72], and the time constants are reported for a least-squares fit to measured data. Parameters and their 95% prediction intervals were estimated by nonlinear least-squares regression (*fitnlm*). The images used in the lymphatic time-series analysis pooled a few groupings (detailed in **Supplementary Table ST1**) of imaging sequence parameters and head rotation positions (positions illustrated in **Extended Data Figure 7a**). The pooling balanced time-course sampling density with the high image-to-image parameter variability. Error bars in **Figure 2d** show the average and standard deviation for images grouped by same acquisition day.

The two-pole overdamped system is modeled as:

$$y = \frac{A\left(e^{-t/\tau_1} - e^{-t/\tau_2}\right)}{(1/\tau_1) - (1/\tau_2)} + C, \tag{2}$$

where $-1/\tau_1$ and $-1/\tau_2$ are distinct real poles, A is the response amplitude and C is an optional constant offset.

Imaging Performance Characterization. The system performance was characterized for spatial resolution, shine-through, and sensitivity using phantoms with both ferumoxytol and ferucarbotran (see **Extended Data Figures 4-6** and **Supplementary Methods** for details).

Spatial resolution was characterized with a Derenzo phantom containing wells of diameter 0.75–2.00 cm, with 0.70 cm depth (**Extended Data Figure 4**). In order to test image resolution at tracer concentrations

that balance tracer signal and system noise, tracers were diluted with saline such that the smallest well (d = 0.75 cm) contained ~10× above the detection limit. Accordingly, ferucarbotran was diluted to 0.3 mg/mL (93 µg/well), and ferumoxytol to 1.6 mg/mL (496 µg/well). Images were acquired for three orientations to capture anisotropic resolution: axial for x/y, two coronal rotations for z and an additional x measurement. Modulation transfer function (MTF) values were then calculated from line profiles by measuring signal at wells and midpoints between wells.

Shine-through performance, which is the ability to resolve a small signal nearby a larger signal source, is tested in phantoms using two configurations. This contrasts with imager dynamic range performance, which is the ratio of the largest to smallest signals that can be imaged in isolation. The first configuration tested the lowest resolution dimensions (x/y) with only the volume coils. A phantom was constructed consisting of an axial spiral arrangement of samples (140 µg ferucarbotran) around a 20× larger tracer source (2.8 mg), at distances of 1.7-6.1 cm, similar to phantom testing performed for Sentimag wand with Magtrace[73]. An image of the phantom was acquired and assessed by inspecting line profiles (**Extended Data Figure 5e**). The second configuration tested anatomically inspired geometries using the lymph node head-and-neck phantom used for benchmarking MPI performance against nuclear medicine (see below). Images were acquired for phantoms containing tracer ratios of 100:1 (**Figure 4**, ferucarbotran and ferumoxytol) and 8000:1 (**Extended Data Figure 6d**, ferucarbotran).

Volume coil sensitivity and linearity vs concentration were assessed using serial 2× dilutions ([72, 36, 18, 9.0, 4.5, 2.3] µg ferucarbotran; [800, 400, 200,100, 50, 25] µg ferumoxytol) for 0.1 mL samples at three positions (n=3) distributed within the field of view to capture any spatial shift variance (**Extended Data Figure 5f,g**). Our reconstruction (MH3D) shapes the image noise statistics, resulting in non-Gaussian and spatially correlated noise. Thus, a suitable metric for detection threshold was defined as the point at which the maximum sample signal, averaged across the three samples (peak signal), matched the image background artifact level (peak background). Peak signal was measured from 3D ROIs centered at each sample, yielding three values per image that were then averaged. The peak background ROI was defined as all values outside the peak signal ROIs. Detection was calculated as the ratio of peak signal to peak background artifact, with detection defined as a ratio $\geq$1.

Application-specific surface coil sensitivity and linearity were assessed using serial 2× dilutions (18 µg–500 ng ferucarbotran) for four samples positioned 1.5 cm from each of four surface coils (**Extended Data Figure 6c**). The surface coils exhibit strong spatial sensitivity variation, which limited our ability to perform consistent detection threshold calculations using MH3D. We found that image processing at the intermediate stage of harmonic portraits ($2f_0$) yielded SNR measures that behaved as expected for Gaussian noise, enabling standard peak SNR (pSNR) measurements. Peak signal was measured from ROIs centered at each sample, yielding four measurements per concentration that were then averaged. pSNR was calculated as the ratio of average peak signal to background standard deviation, with detection defined at pSNR = 3.3 (99.9% confidence).

Imaging Performance Benchmarking with SPECT and Gamma Camera. Phantom studies were completed to benchmark MPI image quality against Tc-99m scintigraphy and SPECT in head and neck lymphatic imaging. A phantom was constructed from a Styrofoam mannequin head (SmoothFōM® Male Foam Head, FloraCraft®, Ludington, Michigan) with holes for a 1.5 mL tube in the left parietal scalp to model the injection site, and eleven 0.2 mL tubes in periauricular and cervical regions to model draining lymph nodes on the same (left). Images were acquired on the phantoms using planar scintigraphy, SPECT, MPI with ferucarbotran and MPI with ferumoxytol. See **Supplementary Methods** for details.

Two replicates of the phantom were built to facilitate imaging across collaborating institutions, but manual

production resulted in 2-4 mm inter-model difference for the lymph node locations in the phantoms used for MPI and for nuclear medicine. Both magnetic and radiotracer phantoms were filled with a 100:1 tracer quantity ratio between the injection site and lymph node vials for comparison.

To prepare the phantom for SPECT and planar scintigraphy, vials were loaded with [^{99m}Tc]tilmanocept (Lymphoseek; Cardinal Health, Dublin, OH, USA) radiotracer. The injection site vial was filled with the FDA-recommended dose[48] of 0.5 mCi in 0.5 mL. The 11× lymph node vials were each filled with 5 µCi, selected based on data from clinical studies that report approximately 0.5–1.8% of injected dose is accumulated[50]. Planar scintigraphy and SPECT imaging (Intevo Bold, SIEMENS) immediately followed phantom preparation. Planar scintigraphy used a 5-minute acquisition, 256 × 256 matrix, LEHR collimator, 140 keV with 15% window but no scatter window setting. SPECT imaging employed 64 stops, 22 sec per stop, non-circular orbit, step and shoot, 128×128 matrix, LEHR collimator, 140 keV with 15% window, and a 15% lower scatter window.

To prepare the phantom for MPI imaging, the vials were filled with ferucarbotran or ferumoxytol magnetic tracer. The injection site vial was filled with 14 mg tracer in 0.5 mL, similar to the injected doses of ferumoxytol used for humans in this study, and to doses used for studies with magnetic tracers Magtrace and Sienna+ for use in melanoma[74] and oral cancer[51]. The 11× lymph node vials were each filled with 140 µg of the corresponding magnetic tracer, based on reported lymph node accumulation[49,51]. In a second experiment, to test the limits of MPI imaging with application-specific receiver coils, ferucarbotran was loaded at a higher ratio of 8000:1, with 56 mg in the injection site vial and 7 µg in each lymph node vial (**Extended Data Figure 6d**). MPI image acquisitions used similar sequences to those used for human imaging and are detailed in **Supplementary Table ST1**.

Preclinical Animal Testing & Tracer Relaxometry. Mouse tracer pharmacokinetics studies were conducted at the Robarts Research Institute under an approved protocol from Western University's Institutional Animal Care and Use Committee (Protocol #2023-113) and adhered to ARRIVE guidelines. Healthy female C57BL/6 mice (12–14 weeks of age, 20–25 g; Charles River) were obtained and cared for in accordance with the standards of the Canadian Council on Animal Care.

Mice received subcutaneous hind-footpad injections of one of three tracers: ferumoxytol manufactured by AMAG Pharmaceuticals (50 µg, n=7), ferumoxytol manufactured by Sandoz (50 µg, n=3), or ferucarbotran (25 µg, n=6) in a volume of 25 µL. Tracer administration was performed using a 30-gauge needle.

MPI images were acquired on a preclinical MPI scanner (Momentum, Magnetic Insight Inc., Alameda, CA) at multiple time points up to 8 weeks post-injection to quantify magnetic tracer pharmacokinetics. For *in vivo* MPI, the imaging field of view was 12 × 6 cm, with multichannel transmit along the x and z axes. The gradient strength was 5.7 T/m, and drive field amplitudes were 20 mT peak (x) and 23 mT peak (z), with a projection scan time of 2 minutes. Images were reconstructed using X-space methods[25,56,57].

MPI signal at injection sites and primary draining lymph nodes were quantified using an ROI with a threshold of $\geq$0.5× maximum intensity. For each timepoint, draining popliteal lymph node and injection site signals were normalized to the baseline MPI signal at the injection site on the ipsilateral limb to compute a percent injected dose (%ID). For time-course analysis, injection site and lymph node time series were fit with the same parametric models as for the human data. Data from all mice within each magnetic tracer group were pooled, and plots report the mean across animals with standard deviation error bars.

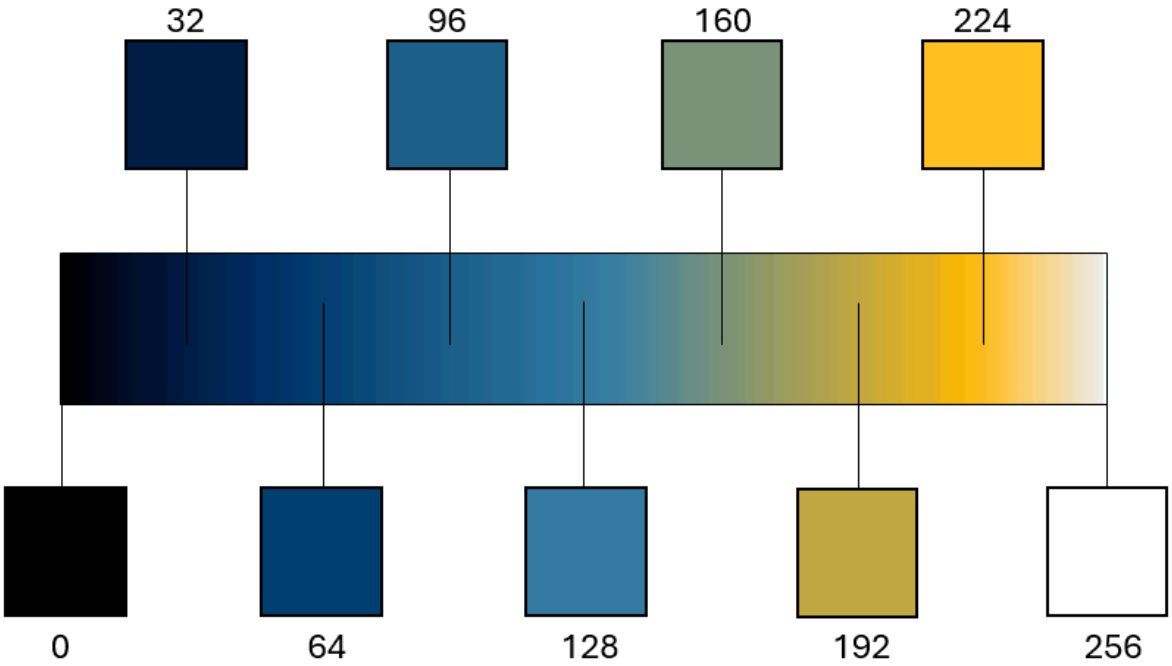
At study endpoint, mice were euthanized and the popliteal and iliac lymph nodes were excised and processed for Perl's Prussian blue staining to confirm iron deposition. The excised lymph nodes were fixed in 4% paraformaldehyde, paraffin-embedded, and sectioned into 5 µm slices.

Magnetic properties of ferumoxytol (AMAG Pharmaceuticals vs. Sandoz) were characterized using magnetic particle relaxometry (RELAX module, Momentum™, Magnetic Insight Inc, Alameda, CA). For relaxometry, ferumoxytol (75 µg) was placed in the center of the imaging holder. This concentration was optimized to produce peak signal = 1 a.u. to provide adequate SNR without saturating the detector. Relaxometry scans were performed using a drive field 20 mT and bias field 160 mT. The point spread functions were normalized to iron concentration for each magnetic tracer.

Supplementary Figures S1-S2



Supplementary Figure S1: Mild skin discoloration following subcutaneous magnetic tracer injection occurred at all injection sites (CTCAE grade 1, <10% body surface area).



Supplementary Figure S2: Visual “bluesteel” color map.

Supplementary Tables ST1-ST2

Supplementary Table ST1: Clinical scanner image scanning parameters and internal identifier (UID).

Unique descriptor	Figure	UID	time after injection [hr]	time after injection [week]	FOVx [m]	FOVy [m]	FOVz [m]	fast shift axis	Ny or Nx	raster step size (dx or dy) [m]	Nz	dz [m]	shift traversals per sec	Drive amplitude [mTp]	app coil center z position [m]	app coil ch1	app coil ch2
S05 head (7.5 mg) coreg	1f	20250318-013429	296.775	1.767	0.22	0.22	0.26	y	46	0.005	53	0.005	4	3.5	-0.1	Left, Bottom	Left, Top
S04 head (15 mg) coreg	1g	20250430-203259	28.516	0.17	0.22	0.22	0.28	y	46	0.005	58	0.005	4	2.8	-0.11	Left, Bottom	Left, Top
S04 head (15 mg) coreg, w/ ROIs	2a	20250430-203259	28.516	0.17	0.22	0.22	0.28	y	46	0.005	58	0.005	4	2.8	-0.11	Left, Bottom	Left, Top
S05 foot (15 mg) coreg	2c (inset)	20250226-181520	1.856	0.011	0.22	0.22	0.2	y	46	0.005	41	0.005	4	3.5	0	N/A	N/A
S04 Foot 1	2c (7.5 mg)	20250113-184909	2.203	0.013	0.22	0.22	0.2	y	46	0.005	41	0.005	4	3.5	0	N/A	N/A
S04 Foot 2	2c (7.5 mg)	20250113-194046	3.063	0.018	0.22	0.22	0.2	y	46	0.005	41	0.005	4	3.5	0	N/A	N/A
S04 Foot 3	2c (7.5 mg)	20250113-203751	4.014	0.024	0.22	0.22	0.2	y	46	0.005	41	0.005	4	3.5	0	N/A	N/A
S04 Foot 4	2c (7.5 mg)	20250113-214609	5.153	0.031	0.22	0.22	0.2	y	46	0.005	41	0.005	4	3.5	0	N/A	N/A
S04 Foot 5	2c (7.5 mg)	20250113-224517	6.138	0.037	0.22	0.22	0.2	y	46	0.005	41	0.005	4	3.5	0	N/A	N/A
S04 Foot 6	2c (7.5 mg)	20250114-000858	7.533	0.045	0.22	0.22	0.2	y	46	0.005	41	0.005	4	3.5	0	N/A	N/A
S04 Foot 7	2c (7.5 mg)	20250114-013815	9.021	0.054	0.22	0.22	0.2	y	46	0.005	41	0.005	4	3.5	0	N/A	N/A
S04 Foot 8	2c (7.5 mg)	20250117-214438	101.127	0.602	0.22	0.22	0.2	y	46	0.005	41	0.005	4	3.5	0	N/A	N/A
S04 Foot 9	2c (7.5 mg)	20250127-173903	337.034	2.006	0.22	0.22	0.2	y	46	0.005	41	0.005	4	3.5	0	N/A	N/A
S04 Foot 10	2c (7.5 mg)	20250415-203451	2211.964	13.166	0.22	0.22	0.2	y	46	0.005	41	0.005	4	3.5	0	N/A	N/A
S04 Foot 11	2c (7.5 mg)	20250415-221540	2213.644	13.176	0.22	0.22	0.2	y	46	0.005	41	0.005	4	3.5	0	N/A	N/A
S04 Foot 12	2c (7.5 mg)	20250723-191419	4586.622	27.301	0.22	0.22	0.2	y	46	0.005	41	0.005	4	3.5	0	N/A	N/A
S04 Foot 13	2c (7.5 mg)	20250723-193104	4586.901	27.303	0.22	0.22	0.2	y	46	0.005	41	0.005	4	3.5	0	N/A	N/A
S04 Foot calibration pad phantom	2c (7.5 mg)	20250114-231246	N/A	N/A	0.22	0.22	0.2	y	46	0.005	41	0.005	4	3.5	0	N/A	N/A
S05 Foot 1	2c (15 mg)	20250226-183149	2.13	0.013	0.22	0.22	0.2	y	46	0.005	41	0.005	4	3.5	0	N/A	N/A
S05 Foot 2	2c (15 mg)	20250226-202916	4.088	0.024	0.22	0.22	0.2	y	46	0.005	41	0.005	4	3.5	0	N/A	N/A
S05 Foot 3	2c (15 mg)	20250227-175929	25.591	0.152	0.22	0.22	0.2	y	46	0.005	41	0.005	4	3.5	0	N/A	N/A
S05 Foot 4	2c (15 mg)	20250228-042743	36.062	0.215	0.22	0.22	0.2	y	46	0.005	41	0.005	4	3.5	0	N/A	N/A
S05 Foot 5	2c (15 mg)	20250228-161649	47.88	0.285	0.22	0.22	0.2	y	46	0.005	41	0.005	4	3.5	0	N/A	N/A
S05 Foot 6	2c (15 mg)	20250228-183231	50.142	0.298	0.22	0.22	0.2	y	46	0.005	41	0.005	4	3.5	0	N/A	N/A
S05 Foot 7	2c (15 mg)	20250304-224819	150.405	0.895	0.22	0.22	0.2	y	46	0.005	41	0.005	4	3.5	0	N/A	N/A
S05 Foot 8	2c (15 mg)	20250312-192334	338.993	2.018	0.22	0.22	0.2	y	46	0.005	41	0.005	4	3.5	0	N/A	N/A
S05 Foot 9	2c (15 mg)	20250722-181050	3505.781	20.868	0.22	0.22	0.2	y	46	0.005	41	0.005	4	3.5	0	N/A	N/A
S05 Foot 10	2c (15 mg)	20250722-184614	3506.371	20.871	0.22	0.22	0.2	y	46	0.005	41	0.005	4	3.5	0	N/A	N/A
S05 Foot 11	2c (15 mg)	20250911-211143	4732.795	28.171	0.22	0.22	0.2	y	46	0.005	41	0.005	4	3.5	0	N/A	N/A
S05 Foot 12	2c (15 mg)	20250911-215405	4733.501	28.176	0.22	0.22	0.2	y	46	0.005	41	0.005	4	3.5	0	N/A	N/A
S05 Foot 13	2c (15 mg)	20250911-220948	4733.763	28.177	0.22	0.22	0.2	y	46	0.005	41	0.005	4	3.5	0	N/A	N/A
S05 Foot calibration pad phantom	2c (15 mg)	20250304-023403	N/A	N/A	0.22	0.22	0.2	y	46	0.005	41	0.005	4	3.5	0	N/A	N/A
S05 Head 1	2b (7.5 mg)	20250305-185453	2.115	0.013	0.22	0.22	0.28	y	46	0.005	58	0.005	4	3.5	0	N/A	N/A
S05 Head 2	2b (7.5 mg)	20250305-210806	4.335	0.026	0.22	0.22	0.28	y	46	0.005	58	0.005	4	3.5	-0.08	Left, Bottom	Left, Top
S05 Head 3	2b (7.5 mg)	20250305-230551	6.298	0.037	0.22	0.22	0.28	y	46	0.005	58	0.005	4	3.5	-0.09	Left, Bottom	Left, Top
S05 Head 4	2b (7.5 mg)	20250306-011612	8.47	0.05	0.22	0.22	0.28	y	46	0.005	58	0.005	4	3.5	-0.08	Left, Bottom	Left, Top
S05 Head 5	2b (7.5 mg)	20250306-180010	25.203	0.15	0.22	0.22	0.28	y	46	0.005	58	0.005	4	3.5	-0.09	Left, Bottom	Left, Top
S05 Head 6	2b (7.5 mg)	20250307-022419	33.605	0.2	0.22	0.22	0.28	y	46	0.005	58	0.005	4	3.5	-0.1	Left, Bottom	Left, Top
S05 Head 7	2b (7.5 mg)	20250307-165235	48.076	0.286	0.22	0.22	0.28	y	46	0.005	58	0.005	4	3.5	-0.1	Left, Bottom	Left, Top
S05 Head 8	2b (7.5 mg)	20250307-191651	50.481	0.3	0.22	0.22	0.28	y	46	0.005	58	0.005	4	3.5	-0.09	Left, Bottom	Left, Top
S05 Head 9	2b (7.5 mg)	20250312-170959	168.366	1.002	0.22	0.22	0.28	y	46	0.005	58	0.005	4	3.5	-0.1	Bilateral, Bottom	Bilateral, Top
S05 Head 10	2b (7.5 mg)	20250317-215722	293.156	1.745	0.22	0.22	0.28	y	46	0.005	58	0.005	4	3.5	-0.1	Left, Bottom	Left, Top
S05 Head 11	2b (7.5 mg)	20250722-203935	3339.86	19.88	0.22	0.22	0.28	y	46	0.005	58	0.005	4	3.5	-0.1	Left, Bottom	Left, Top
S05 Head 12	2b (7.5 mg)	20250723-015010	3345.036	19.911	0.22	0.22	0.28	y	46	0.005	58	0.005	4	3.5	-0.08	Left, Bottom	Left, Top
S05 Head calibration pad phantom	2b (7.5 mg)	20250305-014042	N/A	N/A	0.22	0.22	0.28	y	46	0.005	58	0.005	4	3.5	-0.11	Left, Bottom	Left, Top
S04 Head 1	2b (15 mg)	20250429-192836	3.443	0.02	0.22	0.22	0.28	y	46	0.005	58	0.005	4	2.4	-0.11	Left, Bottom	Left, Top
S04 Head 2	2b (15 mg)	20250429-215150	5.831	0.035	0.22	0.22	0.28	y	46	0.005	58	0.005	4	2.4	-0.11	Left, Bottom	Left, Top
S04 Head 3	2b (15 mg)	20250430-163514	24.554	0.146	0.22	0.22	0.28	y	46	0.005	58	0.005	4	2.4	-0.11	Left, Bottom	Left, Top
S04 Head 4	2b (15 mg)	20250430-233117	31.488	0.187	0.22	0.22	0.28	y	46	0.005	58	0.005	4	2.4	-0.11	Left, Bottom	Left, Top
S04 Head 5	2b (15 mg)	20250501-164333	48.693	0.29	0.22	0.22	0.28	y	46	0.005	58	0.005	4	2.4	-0.11	Left, Bottom	Left, Top
S04 Head 6	2b (15 mg)	20250506-201245	172.179	1.025	0.22	0.22	0.28	y	46	0.005	58	0.005	4	2.4	-0.11	Left, Bottom	Left, Top
S04 Head 7	2b (15 mg)	20250506-204241	172.678	1.028	0.2375	0.22	0.28	y	50	0.005	58	0.005	4	2.4	-0.11	Left, Bottom	Left, Top
S04 Head 8	2b (15 mg)	20250723-215208	2045.836	12.178	0.2375	0.22	0.28	y	50	0.005	58	0.005	4	2.4	-0.11	Left, Bottom	Left, Top
S04 Head calibration pad phantom	2b (15 mg)	20250502-005105	56.818	0.338	0.22	0.22	0.28	y	46	0.005	58	0.005	4	2.4	-0.11	Bilateral, Bottom	Bilateral, Top
S05 Pos3 105/100/110 4-5mm 1	2d (7.5 mg)	20250307-022419	33.605	0.2	0.22	0.22	0.28	y	46	0.005	58	0.005	4	3.5	-0.1	Left, Bottom	Left, Top
S05 Pos3 105/100/110 4-5mm 2	2d (7.5 mg)	20250307-185400	50.1	0.298	0.22	0.22	0.1	y	46	0.005	26	0.004	4	3.5	-0.11	Left, Bottom	Left, Top
S05 Pos3 105/100/110 4-5mm 3	2d (7.5 mg)	20250312-223656	173.816	1.035	0.22	0.22	0.16	y	46	0.005	41	0.004	4	3.5	-0.105	Left, Bottom	Left, Top
S05 Pos3 105/100/110 4-5mm 4	2d (7.5 mg)	20250313-002923	175.69	1.046	0.22	0.22	0.1	y	46	0.005	26	0.004	4	3.5	-0.105	Left, Bottom	Left, Top
S05 Pos3 105/100/110 4-5mm 5	2d (7.5 mg)	20250317-224726	293.991	1.75	0.22	0.22	0.1	y	46	0.005	26	0.004	4	3.5	-0.1	Left, Bottom	Left, Top
S05 Pos3 105/100/110 4-5mm 6	2d (7.5 mg)	20250318-013429	296.775	1.767	0.22	0.22	0.26	y	46	0.005	53	0.005	4	3.5	-0.1	Left, Bottom	Left, Top
S05 Pos3 105/100/110 4-5mm 7	2d (7.5 mg)	20250722-205955	3340.199	19.882	0.22	0.22	0.26	y	46	0.005	53	0.005	4	3.5	-0.1	Left, Bottom	Left, Top
S05 Pos3 105/100/110 4-5mm 8	2d (7.5 mg)	20250722-211715	3340.488	19.884	0.22	0.22	0.1	y	46	0.005	26	0.004	4	3.5	-0.1	Left, Bottom	Left, Top
S05 Pos3 105/100/110 4-5mm 9	2d (7.5 mg)	20250722-235635	3343.143	19.9	0.22	0.22	0.26	y	46	0.005	53	0.005	4	3.5	-0.11	Left, Bottom	Left, Top
S05 Pos3 105/100/110 4-5mm 10	2d (7.5 mg)	20250724-002429	3367.608	20.045	0.22	0.22	0.26	y	46	0.005	53	0.005	4	3.5	-0.1	Left, Bottom	Left, Top
S05 PosN 105/100/110 4-5mm 1	2d (7.5 mg)	20250305-213342	4.762	0.028	0.22	0.22	0.28	y	46	0.005	58	0.005	4	3.5	-0.11	Left, Bottom	Left, Top
S05 PosN 105/100/110 4-5mm 2	2d (7.5 mg)	20250307-165235	48.076	0.286	0.22	0.22	0.28	y	46	0.005	58	0.005	4	3.5	-0.1	Left, Bottom	Left, Top
S05 PosN 105/100/110 4-5mm 3	2d (7.5 mg)	20250307-184534	49.959	0.297	0.22	0.22	0.1	y	46	0.005	26	0.004	4	3.5	-0.11	Left, Bottom	Left, Top
S05 PosN 105/100/110 4-5mm 4	2d (7.5 mg)	20250312-211540	172.461	1.027	0.22	0.22	0.1	y	46	0.005	26	0.004	4	3.5	-0.105	Left, Bottom	Left, Top
S05 PosN 105/100/110 4-5mm 5	2d (7.5 mg)	20250312-221802	173.501	1.033	0.22	0.22	0.14	y	46	0.005	36	0.004	4	3.5	-0.105	Left, Bottom	Left, Top
S05 PosN 105/100/110 4-5mm 6	2d (7.5 mg)	20250312-235242	175.078	1.042	0.22	0.22	0.1	y	46	0.005	26	0.004	4	3.5	-0.105	Left, Bottom	Left, Top
S05 PosN 105/100/110 4-5mm 7	2d (7.5 mg)	20250313-001539	175.461	1.044	0.22	0.22	0.1	y	46	0.005	26	0.004	4	3.5	-0.105	Left, Bottom	Left, Top
S05 PosN 105/100/110 4-5mm 8	2d (7.5 mg)	20250318-021622	297.473	1.771	0.22	0.22	0.26	y	46	0.005	53	0.005	4	3.5	-0.1	Left, Bottom	Left, Top
S05 PosN 105/100/110 4-5mm 9	2d (7.5 mg)	20250722-213851	3340.848	19.886	0.22	0.22	0.26	y	46	0.005	53	0.005	4	3.5	-0.1	Left, Bottom	Left, Top
S05 PosN 105/100/110 4-5mm 10	2d (7.5 mg)	20250722-215419	3341.105	19.888	0.22	0.22	0.1	y	46	0.005	26	0.004	4	3.5	-0.1	Left, Bottom	Left, Top
S05 PosN 105/100/110 4-5mm 11	2d (7.5 mg)	20250724-005132	3368.059	20.048	0.22	0.22	0.1	y	46	0.005	26	0.004	4	3.5	-0.1	Left, Bottom	Left, Top
S04 Pos1 110 1	2d (15 mg)	20250429-211219	5.172	0.031	0.22	0.22	0.18	y	46	0.005	37	0.005	4	2.8	-0.11	Left, Bottom	Left, Top
S04 Pos1 110 2	2d (15 mg)	20250430-205221	28.839	0.172	0.22	0.22	0.28	y	46	0.005	58	0.005	4	2.8	-0.11	Left, Bottom	Left, Top
S04 Pos1 110 3	2d (15 mg)	20250501-195511	51.886	0.309	0.22	0.22	0.28	y	46	0.005	58	0.005	4	2.8	-0.11	Left, Bottom	Left, Top
S04 Pos1 110 4	2d (15 mg)	20250723-223546	2046.563	12.182	0.2375	0.22	0.28	y	50	0.005	58	0.005	4	2.8	-0.11	Left, Bottom	Left, Top
S04 Pos3 110 1	2d (15 mg)	20250429-205620	4.906	0.029	0.22	0.22	0.18	y	46	0.005	37	0.005	4	2.8	-0.11	Left, Bottom	Left, Top
S04 Pos3 110 2	2d (15 mg)	20250430-203259	28.516	0.17	0.22	0.22	0.28	y	46	0.005	58	0.005	4	2.8	-0.11	Left, Bottom	Left, Top
S04 Pos3 110 3	2d (15 mg)	20250430-223403	30.534	0.182	0.22	0.22	0.28	y	46	0.005	58	0.005	4	2.8	-0.11	Left, Bottom	Left, Top
S04 Pos3 110 4	2d (15 mg)	20250501-174207	49.669	0.296	0.22	0.22	0.28	y	46	0.005	58	0.005	4	2.8	-0.11	Left, Bottom	Left, Top
S04 Pos3 110 5	2d (15 mg)	20250723-231853	2047.281	12.186	0.2375	0.22	0.28	y	50	0.005	58	0.005	4	2.8	-0.11	Left, Bottom	Left, Top
S04 PosN 110 1	2d (15 mg)	20250724-163807	2064.602	12.289	0.2375	0.22	0.28	y	50	0.005	58	0.005	4	2.8	-0.11	Left, Bottom	Left, Top
S04 PosN 110 2	2d (15 mg)	20250723-234122	2047.656	12.188	0.2375	0.22	0.28	y	50	0.005	58	0.005	4	2.8	-0.11	Left, Bottom	Left, Top
S04 PosN 110 3	2d (15 mg)	20250723-221616	2046.238	12.18	0.2375	0.22	0.28	y	50	0.005	58	0.005	4	2.8	-0.11	Left, Bottom	Left, Top
S04 PosN 110 4	2d (15 mg)	20250723-215208	2045.836	12.178	0.2375	0.22	0.28	y	50	0.005	58	0.005	4	2.4	-0.11	Left, Bottom	Left, Top
S04 PosN 110 5	2d (15 mg)	20250506-223107	174.485	1.039	0.2375	0.2375	0.28	y	50	0.005	58	0.005	4	2.8	-0.11	Left, Bottom	Left, Top
S04 PosN 110 6	2d (15 mg)	20250506-213352	173.531	1.033	0.2375	0.22	0.18	y	50	0.005	37	0.005	4	2.8	-0.11	Left, Bottom	Left, Top
S04 PosN 110 7	2d (15 mg)	20250501-213518	53.555	0.319	0.22	0.22	0.28	y	46	0.005	58	0.005	4	2.8	-0.11	Left, Bottom	Left, Top
S04 PosN 110 8	2d (15 mg)	20250501-171041	49.145	0.293	0.22	0.22	0.28	y	46	0.005	58	0.005	4	2.8	-0.11	Left, Bottom	Left, Top
S04 PosN 110 9	2d (15 mg)	20250430-233117	31.488	0.187	0.22	0.22	0.28	y	46	0.005	58	0.005	4	2.4	-0.11	Left, Bottom	Left, Top
S04 PosN 110 10	2d (15 mg)	20250430-213808	29.602	0.176	0.22	0.22	0.18	y	46	0.005	37	0.005	4	2.8	-0.11	Left, Bottom	Left, Top
S04 PosN 110 11	2d (15 mg)	20250430-165533	24.893	0.148	0.22	0.22	0.28	y	46	0.005	58	0.005	4	2.8	-0.11	Left, Bottom	Left, Top
S04 PosN 110 12	2d (15 mg)	20250430-163514	24.554	0.146	0.22	0.22	0.28	y	46	0.005	58	0.005	4	2.4	-0.11	Left, Bottom	Left, Top
S04 PosN 110 13	2d (15 mg)	20250429-215150	5.831	0.035	0.22	0.22	0.28	y	46	0.005	58	0.005	4	2.4	-0.11	Left, Bottom	Left, Top
S04 PosN 110 14	2d (15 mg)	20250429-195005	3.801	0.023	0.22	0.22	0.28	y	46	0.005	58	0.005	4	2.4	-0.11	Left, Bottom	Left, Top
100:1 ferucarbotran styrofoam head	4	20250913-002222	N/A	N/A	0.22	0.22	0.28	y	46	0.005	58	0.005	4	3.5	-0.09	Left, Bottom	Left, Top
100:1 ferumoxytol styrofoam head	4	20250905-015110	N/A	N/A	0.22	0.22	0.28	y	46	0.005	58	0.005	4	3.5	-0.09	Left, Bottom	Left, Top
ferucarbotran Derenzo XY	EDF 4b	20250925-224333	N/A	N/A	0.24	0.2375	0.05	y	50	0.005	21	0.003	4	3.5	0	N/A	N/A
ferucarbotran Derenzo XZ 1	EDF 4b	20250926-181933	N/A	N/A	0.24	0.2375	0.24	y	50	0.005	49	0.005	4	3.5	0	N/A	N/A
ferucarbotran Derenzo XZ 2	EDF 4b	20250926-180222	N/A	N/A	0.24	0.2375	0.24	y	50	0.005	49	0.005	4	3.5	0	N/A	N/A
ferumoxytol Derenzo XY	EDF 4c	20250524-010427	N/A	N/A	0.24	0.2375	0.04	y	50	0.005	17	0.003	4	3.5	0	N/A	N/A
ferumoxytol Derenzo XZ 1	EDF 4c	20250524-001401	N/A	N/A	0.24	0.2375	0.24	y	50	0.005	49	0.005	4	3.5	0	N/A	N/A
ferumoxytol Derenzo XZ 2	EDF 4c	20250523-235544	N/A	N/A	0.24	0.2375	0.24	y	50	0.005	49	0.005	4	3.5	0	N/A	N/A
shinethrough	EDF 5e	20240830-210248	N/A	N/A	0.22	0.22	0.05	x	46	0.005	11	0.005	4	3.5	0	N/A	N/A
sensitivity ferucarbotran 70ug	EDF 5fg	20240906-191415	N/A	N/A	0.24	0.226	0.24	y	50	0.005	49	0.005	4	3.5	0	N/A	N/A
sensitivity ferucarbotran 35ug	EDF 5fg	20240906-194001	N/A	N/A	0.24	0.226	0.24	y	50	0.005	49	0.005	4	3.5	0	N/A	N/A
sensitivity ferucarbotran 18ug	EDF 5fg	20240906-200742	N/A	N/A	0.24	0.226	0.24	y	50	0.005	49	0.005	4	3.5	0	N/A	N/A
sensitivity ferucarbotran 9ug	EDF 5fg	20240906-203715	N/A	N/A	0.24	0.226	0.24	y	50	0.005	49	0.005	4	3.5	0	N/A	N/A
sensitivity ferucarbotran 4ug	EDF 5fg	20240906-210541	N/A	N/A	0.24	0.226	0.24	y	50	0.005	49	0.005	4	3.5	0	N/A	N/A
sensitivity ferucarbotran 2ug	EDF 5fg	20240906-213414	N/A	N/A	0.24	0.226	0.24	y	50	0.005	49	0.005	4	3.5	0	N/A	N/A
sensitivity ferumoxytol 800ug	EDF 5fg	20241121-212212	N/A	N/A	0.22	0.22	0.24	y	46	0.005	49	0.005	4	3.5	0	N/A	N/A
sensitivity ferumoxytol 400ug	EDF 5fg	20241121-215231	N/A	N/A	0.22	0.22	0.24	y	46	0.005	49	0.005	4	3.5	0	N/A	N/A
sensitivity ferumoxytol 200ug	EDF 5fg	20241121-221159	N/A	N/A	0.22	0.22	0.24	y	46	0.005	49	0.005	4	3.5	0	N/A	N/A

Supplementary Table ST1: Clinical scanner image scanning parameters and internal identifier (UID) (continued).

sensitivity ferumoxytol 100ug	EDF 5fg	20241121-222925	N/A	N/A	0.22	0.22	0.24	y	46	0.005	49	0.005	4	3.5	0	N/A	N/A
sensitivity ferumoxytol 50ug	EDF 5fg	20241121-224631	N/A	N/A	0.22	0.22	0.24	y	46	0.005	49	0.005	4	3.5	0	N/A	N/A
sensitivity ferumoxytol 25ug	EDF 5fg	20241121-230252	N/A	N/A	0.22	0.22	0.24	y	46	0.005	49	0.005	4	3.5	0	N/A	N/A
surface coil sensitivity ferucabotran 18ug	EDF 6c	20250222-013236	N/A	N/A	0.22	0.22	0.06	y	46	0.005	13	0.005	4	3.5	-0.07	Bilateral, Bottom	Bilateral, Top
surface coil sensitivity ferucabotran 9ug	EDF 6c	20250222-005241	N/A	N/A	0.22	0.22	0.06	y	46	0.005	13	0.005	4	3.5	-0.07	Bilateral, Bottom	Bilateral, Top
surface coil sensitivity ferucabotran 4ug	EDF 6c	20250222-001032	N/A	N/A	0.22	0.22	0.06	y	46	0.005	13	0.005	4	3.5	-0.07	Bilateral, Bottom	Bilateral, Top
surface coil sensitivity ferucabotran 2ug	EDF 6c	20250222-002458	N/A	N/A	0.22	0.22	0.06	y	46	0.005	13	0.005	4	3.5	-0.07	Bilateral, Bottom	Bilateral, Top
surface coil sensitivity ferucabotran 1ug	EDF 6c	20250222-003610	N/A	N/A	0.22	0.22	0.06	y	46	0.005	13	0.005	4	3.5	-0.07	Bilateral, Bottom	Bilateral, Top
surface coil sensitivity ferucabotran 500n	EDF 6c	20250222-004446	N/A	N/A	0.22	0.22	0.06	y	46	0.005	13	0.005	4	3.5	-0.07	Bilateral, Bottom	Bilateral, Top
8000:1 styrofoam head	EDF 6d	20250718-224247	N/A	N/A	0.22	0.22	0.28	y	46	0.005	58	0.005	4	3.5	-0.09	Left, Bottom	Left, Top
rotation1	EDF 7a	20250430-205221	N/A	N/A	0.22	0.22	0.28	y	46	0.005	58	0.005	4	2.8	-0.11	Left, Bottom	Left, Top
rotation2	EDF 7a	20250430-203259	N/A	N/A	0.22	0.22	0.28	y	46	0.005	58	0.005	4	2.8	-0.11	Left, Bottom	Left, Top
rotation3	EDF 7a	20250430-165533	N/A	N/A	0.22	0.22	0.28	y	46	0.005	58	0.005	4	2.8	-0.11	Left, Bottom	Left, Top
positioning1	EDF 7b	20250430-215227	N/A	N/A	0.22	0.22	0.18	y	46	0.005	37	0.005	4	2.8	-0.08	Left, Bottom	Left, Top
positioning2	EDF 7b	20250501-003546	N/A	N/A	0.22	0.22	0.18	y	46	0.005	37	0.005	4	2.8	-0.09	Left, Bottom	Left, Top
positioning3	EDF 7b	20250501-002016	N/A	N/A	0.22	0.22	0.18	y	46	0.005	37	0.005	4	2.8	-0.1	Left, Bottom	Left, Top
positioning4	EDF 7b	20250430-213808	N/A	N/A	0.22	0.22	0.18	y	46	0.005	37	0.005	4	2.8	-0.11	Left, Bottom	Left, Top
Tumor 300ug	EDF 8a	20250311-002955	N/A	N/A	0.22	0.22	0.2	y	46	0.005	41	0.005	4	3.5	0	N/A	N/A
Tumor 600ug	EDF 8a	20250311-012342	N/A	N/A	0.22	0.22	0.2	y	46	0.005	41	0.005	4	3.5	0	N/A	N/A
Tumor 1000ug	EDF 8a	20250311-014124	N/A	N/A	0.22	0.22	0.2	y	46	0.005	41	0.005	4	3.5	0	N/A	N/A
ExtFig8_Perfusion1	EDF 8b	20240401-210951	N/A	N/A	0.22	0.22	0.11	x	46	0.005	56	0.002	8	3.5	0	N/A	N/A
ExtFig8_Perfusion2	EDF 8b	20240401-213732	N/A	N/A	0.22	0.22	0.16	x	46	0.005	81	0.002	8	3.5	0	N/A	N/A
Embo1	EDF 8c	20241221-005327	N/A	N/A	0.2	0.2	0	y	20	0.01	150	0	16	3.5	0	N/A	N/A
Embo2	EDF 8c	20241221-005733	N/A	N/A	0.2	0.2	0	y	20	0.01	150	0	16	3.5	0	N/A	N/A
Embo3	EDF 8c	20241221-010216	N/A	N/A	0.2	0.2	0	y	20	0.01	150	0	16	3.5	0	N/A	N/A

Supplementary Table ST2: "Bluesteel" colormap #255 values, formatted for import into 3D Slicer[61] (label | name | R | G | B | alpha).

0 0 0 0 1 255
1 1 0 2 5 255
2 2 0 4 10 255
3 3 0 6 14 255
4 4 1 8 17 255
5 5 1 9 20 255
6 6 1 11 23 255
7 7 2 13 25 255
8 8 2 14 28 255
9 9 2 16 30 255
10 10 2 17 32 255
11 11 2 18 34 255
12 12 2 19 37 255
13 13 2 20 39 255
14 14 2 21 41 255
15 15 2 22 43 255
16 16 1 23 45 255
17 17 1 24 47 255
18 18 1 25 49 255
19 19 1 26 50 255
20 20 0 27 52 255
21 21 0 28 54 255
22 22 0 28 56 255
23 23 0 29 57 255
24 24 0 30 59 255
25 25 0 31 61 255
26 26 0 32 62 255
27 27 0 33 64 255
28 28 0 34 66 255
29 29 0 34 67 255
30 30 0 35 69 255
31 31 0 36 71 255
32 32 0 37 72 255
33 33 0 38 74 255
34 34 0 39 76 255
35 35 0 40 77 255
36 36 0 40 79 255
37 37 0 41 81 255
38 38 0 42 82 255
39 39 0 43 84 255
40 40 0 44 86 255
41 41 0 45 87 255
42 42 0 45 89 255
43 43 0 46 90 255
44 44 0 47 92 255
45 45 1 48 93 255
46 46 1 49 94 255
47 47 1 50 96 255
48 48 2 51 97 255
49 49 2 52 98 255
50 50 3 53 99 255
51 51 3 53 100 255
52 52 4 54 101 255
53 53 4 55 102 255
54 54 5 56 103 255
55 55 6 57 104 255
56 56 6 58 105 255
57 57 7 59 106 255
58 58 8 60 106 255
59 59 9 61 107 255
60 60 9 62 108 255
61 61 10 63 109 255
62 62 11 64 109 255
63 63 12 65 110 255
64 64 12 66 111 255
65 65 13 67 112 255
66 66 14 68 113 255
67 67 15 68 113 255
68 68 15 69 114 255
69 69 16 70 115 255
70 70 17 71 116 255
71 71 17 72 116 255
72 72 18 73 117 255
73 73 19 74 118 255
74 74 19 75 119 255
75 75 20 76 119 255
76 76 21 77 120 255
77 77 22 78 121 255
78 78 22 78 122 255
79 79 23 79 122 255
80 80 24 80 123 255
81 81 24 81 124 255
82 82 25 82 125 255
83 83 26 83 125 255
84 84 26 84 126 255
85 85 27 85 127 255
86 86 28 86 127 255
87 87 28 86 128 255
88 88 29 87 129 255
89 89 30 88 130 255
90 90 30 89 130 255
91 91 31 90 131 255
92 92 32 91 132 255
93 93 32 92 132 255
94 94 33 92 133 255
95 95 34 93 134 255
96 96 34 94 135 255
97 97 35 95 135 255
98 98 36 96 136 255
99 99 36 97 137 255
100 100 37 97 137 255
101 101 37 98 138 255
102 102 38 99 139 255
103 103 39 100 139 255
104 104 39 101 140 255
105 105 40 101 141 255
106 106 41 102 141 255
107 107 41 103 142 255
108 108 42 104 143 255
109 109 43 105 143 255
110 110 43 106 144 255
111 111 44 106 145 255
112 112 44 107 145 255
113 113 45 108 146 255
114 114 46 109 147 255
115 115 46 110 147 255
116 116 47 110 148 255
117 117 47 111 149 255
118 118 48 112 149 255
119 119 49 113 150 255
120 120 49 113 151 255
121 121 50 114 151 255
122 122 50 115 152 255
123 123 51 116 152 255
124 124 52 116 153 255
125 125 52 117 154 255
126 126 53 118 154 255
127 127 54 119 155 255
128 128 54 120 155 255
129 129 55 120 156 255
130 130 56 121 156 255
131 131 57 122 157 255
132 132 58 123 157 255
133 133 59 123 157 255
134 134 60 124 157 255
135 135 61 125 157 255
136 136 63 126 156 255
137 137 65 126 156 255
138 138 67 127 155 255
139 139 69 128 154 255
140 140 71 129 152 255
141 141 73 129 151 255
142 142 76 130 150 255
143 143 78 131 148 255
144 144 80 132 146 255
145 145 83 132 145 255
146 146 85 133 143 255
147 147 88 134 141 255
148 148 90 134 140 255
149 149 92 135 138 255
150 150 95 136 136 255
151 151 97 136 134 255
152 152 99 137 133 255
153 153 102 138 131 255
154 154 104 138 129 255
155 155 106 139 128 255
156 156 108 140 126 255
157 157 111 140 124 255
158 158 113 141 123 255
159 159 115 142 121 255
160 160 117 142 120 255
161 161 119 143 118 255
162 162 122 144 116 255
163 163 124 144 115 255
164 164 126 145 113 255
165 165 128 145 112 255
166 166 130 146 110 255
167 167 132 147 108 255
168 168 134 147 107 255
169 169 137 148 105 255
170 170 139 148 104 255
171 171 141 149 102 255
172 172 143 150 101 255
173 173 145 150 99 255
174 174 147 151 98 255
175 175 149 152 96 255
176 176 151 152 95 255
177 177 153 153 93 255
178 178 156 153 92 255
179 179 158 154 90 255

180 180 160 155 89 255 195 195 191 163 66 255 210 210 223 173 43 255 225 225 248 185 49 255 240 240 240 209 143 255
181 181 162 155 87 255 196 196 193 164 64 255 211 211 225 173 42 255 226 226 248 187 54 255 241 241 240 211 149 255
182 182 164 156 86 255 197 197 195 165 63 255 212 212 227 174 40 255 227 227 248 188 59 255 242 242 239 212 156 255
183 183 166 156 84 255 198 198 198 165 61 255 213 213 230 174 39 255 228 228 248 190 65 255 243 243 238 214 162 255
184 184 168 157 83 255 199 199 200 166 60 255 214 214 232 175 38 255 229 229 248 191 71 255 244 244 237 215 168 255
185 185 170 158 81 255 200 200 202 166 58 255 215 215 234 176 36 255 230 230 247 193 77 255 245 245 237 217 174 255
186 186 172 158 80 255 201 201 204 167 57 255 216 216 236 176 35 255 231 231 247 195 83 255 246 246 236 218 181 255
187 187 174 159 78 255 202 202 206 168 55 255 217 217 238 177 34 255 232 232 246 196 90 255 247 247 235 220 187 255
188 188 177 159 77 255 203 203 208 168 54 255 218 218 240 178 34 255 233 233 245 198 96 255 248 248 235 221 193 255
189 189 179 160 75 255 204 204 210 169 52 255 219 219 241 179 34 255 234 234 245 200 103 255 249 249 234 222 199 255
190 190 181 160 74 255 205 205 212 170 51 255 220 220 243 180 35 255 235 235 244 201 110 255 250 250 233 224 205 255
191 191 183 161 72 255 206 206 215 170 49 255 221 221 244 181 36 255 236 236 243 203 116 255 251 251 232 225 211 255
192 192 185 162 71 255 207 207 217 171 48 255 222 222 245 182 38 255 237 237 243 204 123 255 252 252 232 227 217 255
193 193 187 162 69 255 208 208 219 171 46 255 223 223 246 183 41 255 238 238 242 206 130 255 253 253 231 228 223 255
194 194 189 163 68 255 209 209 221 172 45 255 224 224 247 184 45 255 239 239 241 208 136 255 254 254 230 229 229 255

Supplementary Videos SV1-SV2

Supplementary Video SV1: Video of tomographic MPI images co-registered with de-indentified surface scans (see **Figure 1f,g**).
File: *SV1.mp4*.

Supplementary Video SV2: Real-time 2D axial slice imaging at 0.8 frames/second of a trans-arterial embolization liver phantom being filled with ferucarbotran (see **Extended Data Figure 8b**).
File: *SV2.mp4*.

Supplementary Data SD1-SD2

Supplementary Data SD1: 3D Slicer[61] scene for tomographic MPI image co-registered with de-indentified surface scan. Image of subject with 7.5 mg ferumoxytol injection at t = 12.4 days, with two fiducials (Fid) containing 0.5 mg ferumoxytol (see **Figure 1f**).
File: *SD1_scene_S05_2025-08-12.mrb*.

Supplementary Data SD2: 3D Slicer[61] scene for tomographic MPI image co-registered with de-indentified surface scan. Image of subject with 15 mg ferumoxytol injection at t = 28.5 hours, no fiducials used (see **Figure 1g**).
File: *SD2_Scene_S04_2025-08-19.mrb*.

Supplementary Files

This is a list of supplementary files associated with this preprint. Click to download.

- SV1.mp4
- SV2.mp4